Bose-Einstein Correlations of Charged Kaons and Pions in Central Pb+Pb Collisions at 158 AGeV

Dissertation
zur
Erlangung des Doktorgrades
der Naturwissenschaften
(Dr. rer. nat.)

dem
Fachbereich Physik
der Philipps-Universität Marburg
vorgelegt von

In-Kwon YOO

aus Seoul, Korea

Marburg/Lahn 2001

Vom Fachbereich Physik der Philipps-Universität Marburg als Dissertation angenommen am : 14. Februar 2001

Erstgutachter : Prof. Dr. F. Pühlhofer, Universität Marburg

Zweitgutachter : Prof. Dr. H. Ströbele, Universität Frankfurt a.M.

Tag der mündlichen Prüfung am : 05. März 2001

To Hee-Kyeong, Minsu and my Mother

Zusammenfassung

Forschungsgegenstand der experimentellen Hochenergie-Schwerionenphysik ist das Verhalten hadronischer Materie bei sehr hohen Energiedichten. Gesucht wird eine neue Materieform, das sogenannte Quark-Gluon-Plasma (QGP). In diesem Zustand liegen die Quarks nicht mehr in Hadronen gebunden, sondern in einem größeren Raum-Zeit-Volumen quasi-frei vor. Allerdings ist dieser Zustand nur bei hoher Energiedichte zu erwarten.

Auf dieser Motivation beruht das NA49-Experiment am CERN-SPS-Beschleuniger, mit dem Stöße zwischen Pb-Kernen bei 158 GeV pro Nukleon untersucht werden. Die dabei erreichte Energiedichte liegt in einem Bereich, indem der Phasenübergang vermutet wird. Den Ablauf der Reaktion versucht man mit Hilfe der bei der Kollision emittierten Teilchen zu rekonstruieren. Diese werden in NA49 mit einem Hadronenspektrometer großer Akzeptanz nachgewiesen.

Betrachtet man dabei die Verteilung der Impulsdifferenzen detektierter Teilchen, dann ist im Falle von Bosonen eine Überhöhung der Häufigkeit bei kleinen Werten beobachtbar, die von der Bose-Einstein-Korrelation verursacht wird (sog. HBT-Effekt). Nach der Heisenberg'schen Unschärferelation hängt die Breite dieser gaußförmigen Überhöhung mit der raumzeitlichen Ausdehnung der Reaktionszone zusammen.

Das Hauptziel dieser Arbeit ist die Untersuchung und der Vergleich der raumzeitlichen Konfiguration der Quelle für Kaonen und Pionen in zentralen Pb+Pb Kollisionen bei 158 GeV/u. Wegen unterschiedlicher Wechselwirkungsquerschnitte und unterschiedlicher Beiträge kurzlebiger Resonanzen ist der Vergleich zwischen Kaonen und Pionen interessant. Da sich die Bildung eines QGP auf die Expansion der Reaktionszone auswirkt, damit auch auf die Konfiguration, bei der die Teilchen-

Entkopplung stattfindet, erhält man indirekt eine Information über den Phasenübergang.

Im Experiment werden etwa zehnmal weniger Kaonen als Pionen produziert. Damit diese seltenen Kaonen bei mittlerer Rapidität mit möglichst wenig Kontamination identifiziert werden können, wird der NA49-Flugzeitdetektor benutzt. Die zum Vergleich benötigten Pionen mittlerer Rapidität haben wesentlich geringere Impulse. Sie sind nur durch die $\mathrm{d}E/\mathrm{d}x$-Methode selektierbar.
Mit den so gewonnenen Daten wird die HBT-Analyse sowohl eindimensional, als auch dreidimensional durchgeführt. Hierbei ist die Coulomb-Abstoßung zwischen gleich geladenen Teilchen durch die analytische Coulombfunktion korrigiert, deren Parameter aus der Coulomb-Korrelation zwischen ungleich geladenen Teilchen extrahiert wurden.
Aus den resultierenden Radien von Kaonen und Pionen, die nach der Yano-Koonin-Podgoretskii-Parameterisierung die transversale und longitudinale Ausdehnung der Quelle und die Emissionsdauer der Teilchen charakterisieren, folgt :

- Für die räumliche und zeitliche Ausdehnung der Reaktionszone am Ausfrierzeitpunkt werden mit Kaonen und Pionen etwa die gleichen Werte bestimmt. Dies deutet an, daß sich unterschiedliche Wirkungsquerschnitte und Bildungsmechanismen nicht auf das Meßergebnis auswirken.

- Im Rahmen des hydrodynamischen Modells kann die Lebensdauer des Systems zu ca. 10 fm/c für beide Teilchen mit mittlerer Rapidität abgeschätzt werden. Tritt ein Phasenübergang erster Ordnung auf, wird latente Wärme erzeugt, währenddessen das QGP und das Hadronengas koexistieren, was zu einer längeren Lebensdauer führt als bei einem Szenario ohne Phasenübergang. Das gemessene relativ lang verzögerte Ausfrieren beider Teilchen ($\tau_f \approx 10 \pm 1.5$ fm/c) stimmt mit der theoretischen Vorhersage überein.

- Vergleicht man die Radien von positiven und negativen Teilchen, sieht man den zentralen Coulombeffekt, der von der positiv geladenen Quellen verursacht wird.

- Die longitudinalen Radien nehmen in Abhängigkeit von den transversalen Massen stärker ab als die transversalen Radien. Dies ist konsistent damit, daß die Expansion in Strahlrichtung viel stärker ist als in transversaler Richtung.

Abstract

NA49 is a large-acceptance spectrometer for the investigation of hadron production in 158 AGeV Pb+Pb collisions at the CERN-SPS. It is generally expected that the conventional hadronic degrees of freedom governing normal nuclear matter are melted away as a consequence of the high energy densities reached in these collisions, thus forming a new state of matter, the quark-gluon plasma (QGP). In order to verify experimentally whether a phase transition to such a state occurs, it is important to characterize the relevant properties of the source that is formed in the collisions. This thesis explores the geometrical and dynamical properties of the reaction zone produced in the central Pb+Pb collisions by means of Hanbury-Brown and Twiss (HBT) intensity interferometry.

The freeze-out configurations of kaons and of pions, both from the central rapidity region, are extracted by 1-dimensional and 3-dimensional HBT analyses.

It is found, that the freeze-out configuration of kaons is very similar to that of pions. Particularly the relatively long and similar freeze-out proper time, which is extracted from the $m_{\perp}$-dependence of the longitudinal radii, is consistent with hydrodynamical reaction models that include a phase transition.

keywords : *NA49, quark-gluon-plasma (QGP), HBT intensity interferometry, freeze-out configuration, freeze-out proper time, expansion of source*

Contents

Chapter 1

Introduction

1.1 Hadronic Matter under Extreme Conditions

In the early 1960s the quark model was suggested by Gell-Mann [Gel64] and Zweig [Zwe64] for the hadronic substructure. In this model, mesons are to be described as quark-antiquark bound states ($q\bar{q}$), and baryons as three-quark bound states(qqq). Experimentally, however, no single quark, described by a color triplet state, has ever been isolated ; only the colorless hadrons are observed. This "confinement" of the quarks inside the hadrons suggests that the interaction between them must be very strong on large distance scales.

For mesons, an intuitive way to visualize the confinement is the picture of a field tube between a quark and an antiquark containing a constant strong interaction field. As the separation between the quark and antiquark becomes large, the energy of the field increases linearly and, at some point, it becomes energetically more favorable to produce another quark-antiquark pair at a point along the tube such that the produced quark is connected to the antiquark while the produced antiquark is connected to the quark. To isolate a quark from its antiquark partner would then be impossible.

With quarks being confined inside a hadron, a useful phenomenological description of quarks in hadrons is provided by the *(MIT) Bag Model* [Cho74]. In the model, quarks are treated as massless particles inside a bag, and are infinitely massive outside the bag. In the model, confinement is the result of the balance of the *bag*

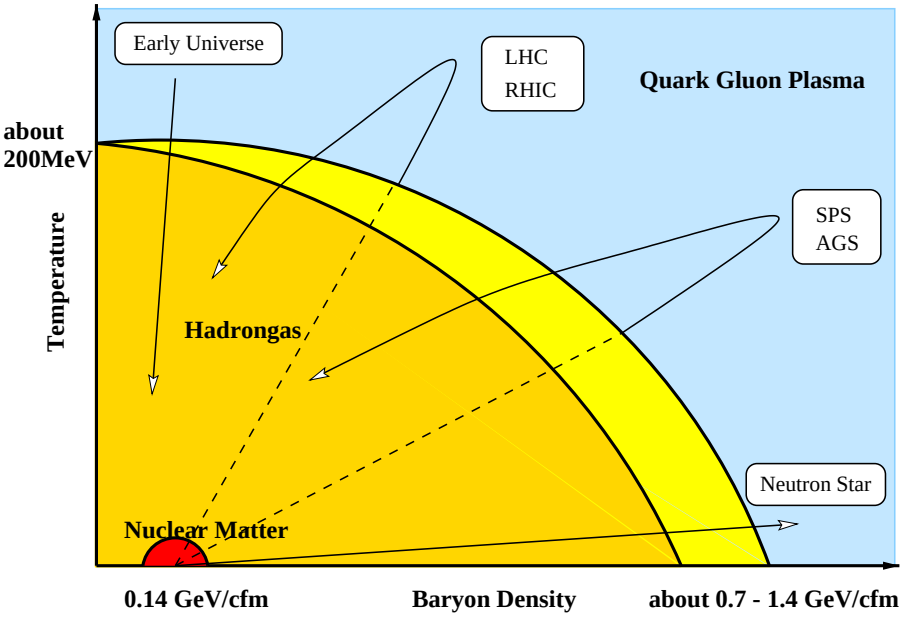

Fig. 1.1: Phase diagram in the plane of the temperature and the net baryon density. At a high enough temperature (energy density) or net baryon density (matter density), hadronic matter may undergo a phase transition where properties could be quite different. [Sch92]

pressure B, which is directed inward, and the stress arising from the kinetic energy of the quarks. If the quarks are confined in the bag, this should also hold for the gluons. In this picture, the total color charge of the matter inside the bag must vanish. Since there are three different types of color, the bag model would imply that the allowable hadronic bags should include colorless qqq or $q\bar{q}$ states.

In order to discuss matter under extreme conditions, it is useful to use this model as a starting point. If the pressure of the quark matter within the bag is sufficiently increased, there should be a point where the outward pressure will exceed the inward pressure. At that point, the bag pressure cannot balance the outward quark matter pressure and the bag cannot confine the quark matter contained inside. A new phase of matter containing the quarks and gluons in an unconfined state, **the Quark-Gluon-Plasma (QGP)** will then be possible. The situation now leads to the possible existence of different phases of the quark matter. The main condition for a new phase of quark matter is the occurrence of a large pressure exceeding the bag pressure B.

A large pressure arises :

1) when the temperature of the matter is high and/or

2) when the baryon number density is large.

New phases of quark matter are then expected [Won94] [Mue85]. This relation is more noticeable in the phase diagram of strong-interacting matter (Fig. 1.1).
The early Universe presumably underwent this phase transition 10^{-5} s after the Big Bang. Contrarily, the dynamics of supernova explosions and the stability of neutron stars depend on the compressibility and it is even speculated that the core of neutron stars may consist of cold QGP as shown in Fig. 1.1. In the laboratory condition, such hot and dense hadronic matter may be artificially reached in ultrarelativistic heavy-ion collisions. In this respect, the CERN-SPS is presently one of the most powerful facilities, where a ^{208}Pb-beam with 158 AGeV is offered giving the center-of-mass energy 17.3 GeV in the NN-system.

1.2 High-Energy Heavy-Ion Collisions

As the simplest case, we consider the head-on collision of two equal nuclei in the center-of-mass frame. Due to the substantial Lorentz contraction in the longitudinal direction, we can represent the two colliding nuclei by two thin disks. The configuration of the two nuclei before collision in the center-of-mass frame is illustrated in Fig. 1.2 (a). Considering the extreme high-energy case, the projectile nucleus B coming from $z = -\infty$ meets the target nucleus A which comes from $z = +\infty$ at a speed close to the speed of light. They meet at $z = 0$ and $t = 0$. From the experimental data, it is known that each inelastic nucleon-nucleon collision is accompanied by a large energy loss of the colliding baryons [Won94]. At very high energies, the slowed-down baryons after the collision can still have enough momentum to proceed forward, and move away from the region of collision (Fig. 1.2 (b)), where the projectile baryon matter after the collision is denoted by B' and the target baryon matter by A'. The energy-loss by the baryons is deposited in a small region of space around $z = 0$ in a short duration of time.
The dynamics can be viewed from a different perspective in the space-time diagram (Fig. 1.3). At the point of $(z, t) = (0, 0)$, collisions between the nucleons of the projectile nucleus and the nucleons of the target nucleus take place. The energy deposited in the collision region around $z \sim 0$ can be quantized in the form of quarks,

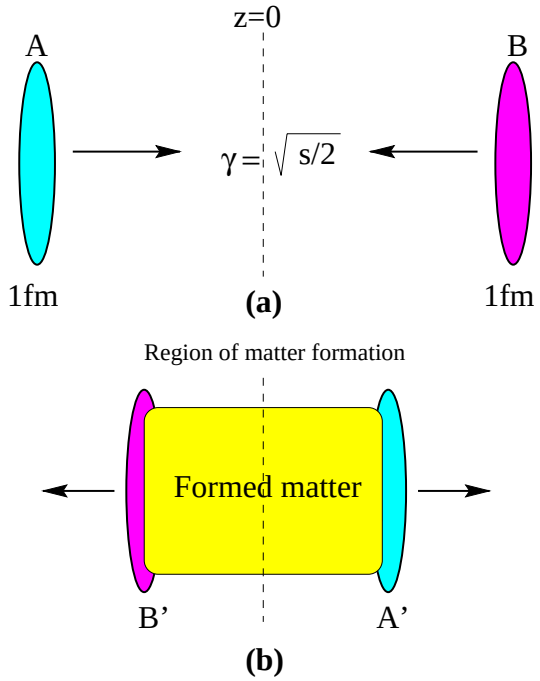

Fig. 1.2: (a) The configuration of two colliding nuclei A and B *before* collision. (b) The configuration *after* collision with energy deposited in the region around $z \sim 0$. (according to [Bjo83])

gluons, or hadrons. As illustrated in Fig. 1.3, there may be two different scenarios with and without the QGP formation, in accordance with the deposited energy density around $z \sim 0$. Soon after the collision of the two nuclei at $(z, t) = (0, 0)$, the energy density may be high enough to form the quark-gluon plasma in the central rapidity region. The plasma initially may not be in thermal equilibrium, but will be subsequently equilibrated at the proper time τ_0, and the plasma may then evolve according to the laws of hydrodynamics thereafter. As the plasma expands, its temperature drops down and the hadronization of the plasma will take place at a later proper time. When the temperature falls below the "freeze-out" temperature at the time τ_f, the interactions between the produced hadrons will finally end (*freeze-out*), and the hadrons will stream out of the collision region. The spatial and temporal configuration at this moment is called *freeze-out configuration of hadrons*.

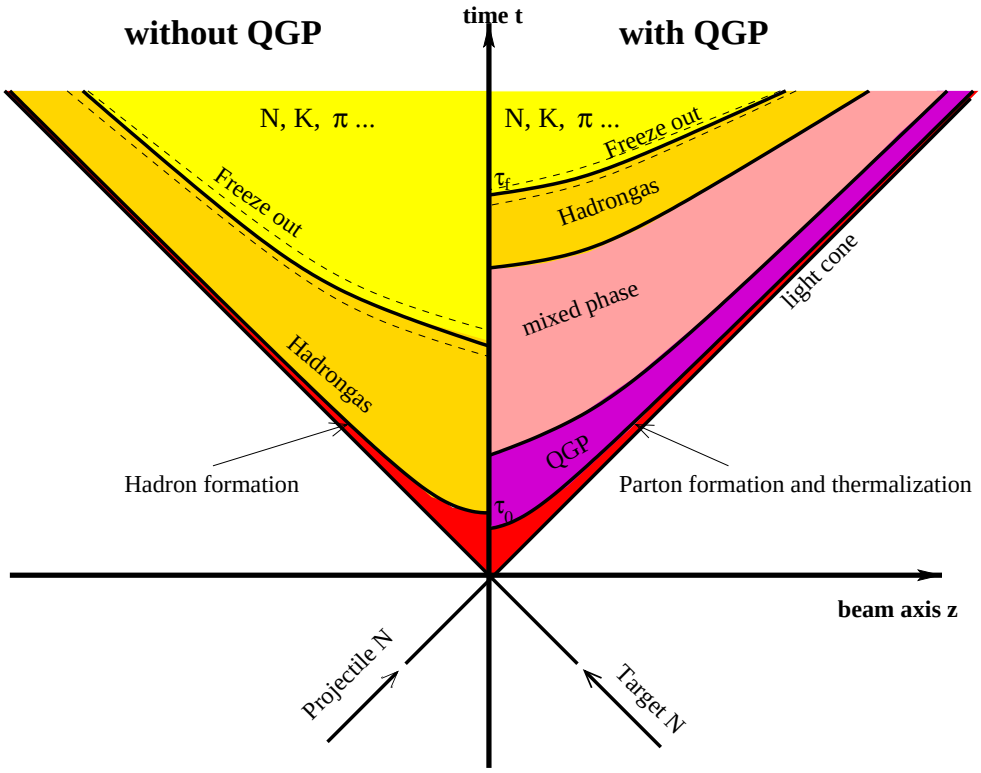

Fig. 1.3: The space-time scenario for a high-energy nucleus-nucleus collision is shown with QGP formation (right) and without (left), respectively. The two scenarios may coexist in the same event.[Son94]

1.3 Searching for the Quark-Gluon Plasma Phase Transition

Subsequent cooling allows the matter to return to the hadron phase and to appear as hadrons, which can be detected in the experiment. These particles from the interaction between the constituents of the plasma will then provide information concerning the state of the plasma, if there was a priori the quark-gluon plasma. The detection of the products of their interactions is, therefore, a plasma diagnostic tool. There have been many suggestions from theory, and several possible signatures for the phase transition are described below.

As suggested by Rafelski [Raf82], the strangeness enhancement is one of the possible signatures. In the heavy-ion collision, the lightest and dominant hadron is the pion, which is composed of the two lightest quarks, u and d. If hadronic densities become

large enough, the chemical potential of the u ($m_u \simeq 5$ MeV) and d ($m_d \simeq 10$ MeV) quarks can become the order of the strange quark mass ($m_s \simeq 150$ MeV), since the chemical potential is proportional to the hadronic density [Raf92]. In addition, the chemical equilibrium to produce the strange quarks is reached in QGP 10-30 times sooner than in the hadronic gas. As a combined result, it becomes energetically favorable to thermally produce strange (s) quarks rather than the lighter flavors, resulting an increase of strange hadrons. The strangeness enhancement is then quantifiable in a ratio of strange to non-strange hadrons (i.e. $\frac{K}{\pi}$, $\frac{\Lambda}{p}$, etc.). Such has been studied in many previous experiments and is an important component in the NA49 research program [Afa00].

The opposite of strangeness enhancement is the J/ψ suppression, as suggested by Satz and Matsui [Mat86]. In a quark-gluon plasma, a color charge of a quark is subject to be screened by the presence of quarks, antiquarks, and gluons in the plasma. This phenomenon is called *Debye screening*. In case of the J/ψ meson, which is composed of a charm quark c and an antiquark $\bar{c}$ with $m_{J/\psi} \simeq 3.1$ GeV, the Debye screening in the plasma will weaken the interaction between c and $\bar{c}$. Therefore, a J/ψ particle in the quark-gluon plasma at high temperatures will become dissociated. This will increase the rate of production of open charm mesons (i.e. D mesons) and decrease the J/ψ yield. Experimentally the J/ψ production is being investigated with relation to open charm mesons in CERN Pb+Pb collisions [Gaz99].

With the above signatures, the spatial and temporal characterizations of the particle production source is an important component in understanding the evolution of heavy-ion collisions. In relativistic heavy-ion collisions the momenta of the escaping hadrons are determined at the point of "freeze out". They should carry information about the final state of the fireball which can be use to reconstruct this state and thus obtain boundary conditions for back-extrapolation into earlier stages of its evolution. In this way one can examine the question whether a quark-gluon plasma was created or not. For instance, an anomalously long lifetime of the source could signal the presence of a system that has a latent heat associated with it. If the source were expanding, it would have a large spatial extention. In particular, a comparison of such configurations of pions to those of kaons can give us remarkable informations concerning model dependent scenarios (see section 2.3). The following chapters will detail the characterization of the spatial-temporal extensions of the average source created in central Pb+Pb collisions at 158 AGeV using particle interferometry.

Chapter 2

Particle Interferometry and the HBT Effect

Interference is a well-known wave phenomenon associated with the superposition of two or more waves. For example, the appearance of Young's diffraction pattern in a two-slit experiment is the result of the interference of the amplitudes of two light waves from two slit openings which travel in different paths to arrive at the same detection point.

There is another wave interference phenomenon, which is associated with the interference of the intensities when identical particles are detected at different space-time points or energy-momentum points.

This new kind of interferometry was formulated in the mid-1950s by Hanburry-Brown and Twiss (HBT) [Han54]. This so-called HBT interferometry was first applied in astronomy in order to deduce the spatial extension of stars. Shortly after its development, it was shown that the effect is universal and could be observed for any emitting source [Han56]. The first application to particle physics has been proposed and successfully carried out by G. Goldhaber, S. Goldhaber, Lee and Pais (GGLP) in order to measure the space-time dimensions in $p\bar{p}$ annihilation [Gol60].

The HBT-Effect is caused by the principles of quantum statistics for indistinguishable particles. In the case of bosons, there is an attraction (or a correlation) between identical particles in phase space, whereas fermions exhibit the opposite behavior, producing a repulsion (or an anti-correlation) between particles. Both effects have

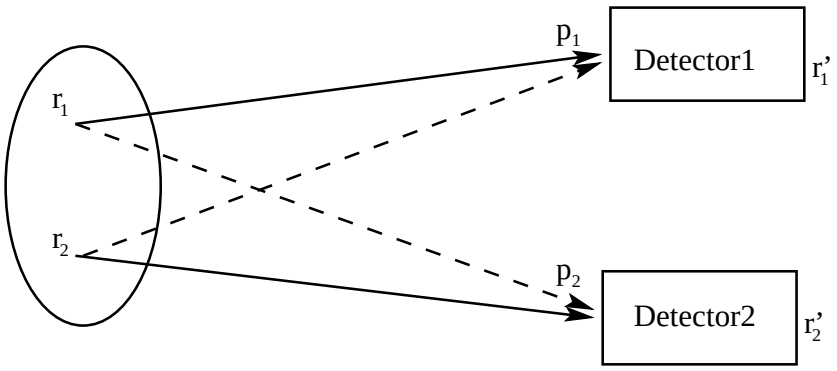

Fig. 2.1: A measurement cannot distinguish which particle is from the space-time point r_1 and which is from r_2.

been seen experimentally and have allowed estimates of the space-time structure of subatomic collisions.

2.1 Two-Particle Correlation Function

According to Heisenberg's uncertainty relation ($\Delta p \Delta r \simeq \hbar$), momentum and position cannot be precisely measured at the same time. Therefore, for a given momentum difference of two particles we cannot determine where in the emitting source they exactly come from.

Now we consider the two-particle momentum distribution $P(\mathsf{p}_1, \mathsf{p}_2)$, defined as the probability distribution for two particles of momenta p_1 and p_2, to be produced from the extended source and to arrive at their respective detection points $\mathsf{r'}_1$ and $\mathsf{r'}_2$ (Fig. 2.1).[1]

Assuming that the probability amplitude for the production of the particle with momentum p_i at r_i is given by $A(\mathsf{p}_i, \mathsf{r}_i)e^{i\phi(\mathsf{r}_i)}$, the probability amplitude of two particles to be produced and propagate from the source point to the detection point is (solid lines in Fig. 2.1):

$$A(\mathsf{p}_1, \mathsf{r}_1)e^{i\phi(\mathsf{r}_1)}\psi(\mathsf{p}_1 : \mathsf{r}_1 \to \mathsf{r'}_1)A(\mathsf{p}_2, \mathsf{r}_2)e^{i\phi(\mathsf{r}_2)}\psi(\mathsf{p}_2 : \mathsf{r}_2 \to \mathsf{r'}_2) \tag{2.1}$$

[1] where p_i and r_i denote the four-momentum and the space-time four-vector of particle i, respectively.

which can be expressed as

$$A(\mathsf{p}_1,\mathsf{r}_1)e^{i\phi(\mathsf{r}_1)}e^{i\mathsf{p}_1\cdot(\mathsf{r}_1-\mathsf{r'}_1)}A(\mathsf{p}_2,\mathsf{r}_2)e^{i\phi(\mathsf{r}_2)}e^{i\mathsf{p}_2\cdot(\mathsf{r}_2-\mathsf{r'}_2)}. \tag{2.2}$$

However, this is not the only probability amplitude contribution for two identical particles produced from r_1 and r_2 to arrive at $\mathsf{r'}_1$ and $\mathsf{r'}_2$. The particle of momentum p_1 detected at $\mathsf{r'}_1$ can also be produced at r_2 and propagate from r_2 to $\mathsf{r'}_1$. The other identical particle of momentum p_2 detected at $\mathsf{r'}_2$ can be produced at r_1 and propagate from r_1 to $\mathsf{r'}_2$ as indicated by the dashed lines in Figure 2.1. The probability amplitude for this occurrence is

$$A(\mathsf{p}_1,\mathsf{r}_2)e^{i\phi(\mathsf{r}_2)}\psi(\mathsf{p}_1:\mathsf{r}_2\to\mathsf{r'}_1)A(\mathsf{p}_2,\mathsf{r}_1)e^{i\phi(\mathsf{r}_1)}\psi(\mathsf{p}_2:\mathsf{r}_1\to\mathsf{r'}_2) \tag{2.3}$$

which can be expressed as

$$A(\mathsf{p}_1,\mathsf{r}_2)e^{i\phi(\mathsf{r}_2)}e^{i\mathsf{p}_1\cdot(\mathsf{r}_2-\mathsf{r'}_1)}A(\mathsf{p}_2,\mathsf{r}_1)e^{i\phi(\mathsf{r}_1)}e^{i\mathsf{p}_2\cdot(\mathsf{r}_1-\mathsf{r'}_2)}. \tag{2.4}$$

Because of the indistinguishability and the Bose-Einstein statistics of bosons, the probability amplitude must be symmetrical with respect to the interchange of the labels [2] r_1 and r_2. In contrast, for identical fermions the probability amplitude must be anti-symmetrical. Accordingly, the probability amplitude which satisfies this (anti)symmetry is the sum(difference) of Eq. 2.2 and Eq. 2.4 divided by $\sqrt{2}$:

$$\frac{1}{\sqrt{2}}\Big\{A(\mathsf{p}_1,\mathsf{r}_1)e^{i\phi(\mathsf{r}_1)}e^{i\mathsf{p}_1\cdot(\mathsf{r}_1-\mathsf{r'}_1)}A(\mathsf{p}_2,\mathsf{r}_2)e^{i\phi(\mathsf{r}_2)}e^{i\mathsf{p}_2\cdot(\mathsf{r}_2-\mathsf{r'}_2)} \tag{2.5}$$

$$\pm A(\mathsf{p}_1,\mathsf{r}_2)e^{i\phi(\mathsf{r}_2)}e^{i\mathsf{p}_1\cdot(\mathsf{r}_2-\mathsf{r'}_1)}A(\mathsf{p}_2,\mathsf{r}_1)e^{i\phi(\mathsf{r}_1)}e^{i\mathsf{p}_2\cdot(\mathsf{r}_1-\mathsf{r'}_2)}\Big\}$$

$$\equiv e^{i\phi(\mathsf{r}_1)}e^{i\phi(\mathsf{r}_2)}\Phi(\mathsf{p}_1\mathsf{p}_2:\mathsf{r}_1\mathsf{r}_2\to\mathsf{r'}_1\mathsf{r'}_2) \tag{2.6}$$

where Φ is the ϕ-independent part of the probability amplitude.

We will consider only the case of bosons, because we are only interested in the case of kaons and pions.[3]

Integrating Eq. 2.5 over all the source points with the source density function $\rho(\mathsf{r}_i)$, we get the two-particle distribution for a chaotic source as :

$$P(\mathsf{p}_1,\mathsf{p}_2)=\int \mathrm{d}\mathsf{r}_1\mathrm{d}\mathsf{r}_2\rho(\mathsf{r}_1)\rho(\mathsf{r}_2)|\Phi(\mathsf{p}_1\mathsf{p}_2:\mathsf{r}_1\mathsf{r}_2\to\mathsf{r'}_1\mathsf{r'}_2)|^2. \tag{2.7}$$

[2] In this case, the only labels which distinguish the two identical bosons are the source points r_1 and r_2, because one boson of momentum p_1 has been determined to have been detected at $\mathsf{r'}_1$ and the other identical boson of momentum p_2 at $\mathsf{r'}_2$.

[3] In case of fermions we can simply replace the plus sign with the minus sign for interchanging the labels.

Substituting Eq. 2.5 into Eq. 2.7 leads to :

$$P(\mathsf{p}_1,\mathsf{p}_2) = P(\mathsf{p}_1)P(\mathsf{p}_2) + \Big|\int \mathrm{d}\mathsf{r} e^{i(\mathsf{p}_1-\mathsf{p}_2)\cdot\mathsf{r}}\rho(r)A(\mathsf{p}_1,\mathsf{r})A(\mathsf{p}_2,\mathsf{r})\Big|^2 \tag{2.8}$$

where $P(\mathsf{p}_i) \equiv \int \mathrm{d}\mathsf{r}_i \rho(\mathsf{r}_i)A^2(\mathsf{p}_i,\mathsf{r}_i)$. Introducing the *effective density function* defined as

$$\rho_{eff}(\mathsf{r};\mathsf{p}_1\mathsf{p}_2) \equiv \frac{\rho(\mathsf{r})A(\mathsf{p}_1,\mathsf{r})A(\mathsf{p}_2,\mathsf{r})}{\sqrt{P(\mathsf{p}_1)P(\mathsf{p}_2)}} \tag{2.9}$$

and its Fourier transform $\tilde{\rho}_{eff}(\mathsf{q};\mathsf{p}_1\mathsf{p}_2)$ defined as

$$\tilde{\rho}_{eff}(\mathsf{q};\mathsf{p}_1\mathsf{p}_2) = \int \mathrm{d}\mathsf{r} e^{i\mathsf{q}\cdot\mathsf{r}}\rho_{eff}(\mathsf{r};\mathsf{p}_1\mathsf{p}_2), \tag{2.10}$$

where $\mathsf{q} \equiv \mathsf{p}_1 - \mathsf{p}_2$. The two-particle momentum distribution function is, then, a function of $\tilde{\rho}_{eff}(\mathsf{q};\mathsf{p}_1\mathsf{p}_2)$ as

$$P(\mathsf{p}_1,\mathsf{p}_2) = P(\mathsf{p}_1)P(\mathsf{p}_2)\big(1+|\tilde{\rho}_{eff}(\mathsf{q};\mathsf{p}_1\mathsf{p}_2)|^2\big). \tag{2.11}$$

Finally, the *correlation function* $C_2(\mathsf{p}_1,\mathsf{p}_2)$ is defined as the ratio of the probability for the coincidence of p_1 and p_2 relative to the probability of observing p_1 and p_2 separately,[4]

$$C_2(\mathsf{p}_1,\mathsf{p}_2) = \frac{P(\mathsf{p}_1,\mathsf{p}_2)}{P(\mathsf{p}_1)P(\mathsf{p}_2)} = 1 + |\tilde{\rho}_{eff}(\mathsf{q};\mathsf{p}_1\mathsf{p}_2)|^2. \tag{2.12}$$

Replacing $\rho(\mathsf{r})A^2(\mathsf{p},\mathsf{r})$ in Eqs. 2.9, 2.10 and 2.12 with *the source emission function* $S(\mathsf{p},\mathsf{r})$, which means the phase space distribution function and the classical analogue of the quantum mechanical Wigner function, we can approximately get :

$$C_2(\mathsf{p}_1,\mathsf{p}_2) \equiv C_2(\mathsf{q},\mathsf{K}) \cong 1 + \frac{|\int \mathrm{d}\mathsf{r} S(\mathsf{r},\mathsf{K})e^{i\mathsf{q}\cdot\mathsf{r}}|^2}{|\int \mathrm{d}\mathsf{r} S(\mathsf{r},\mathsf{K})|^2}, \tag{2.13}$$

where we use $\mathsf{q} = \mathsf{p}_1 - \mathsf{p}_2$ and $\mathsf{K} = \frac{1}{2}(\mathsf{p}_1 + \mathsf{p}_2)$ instead of the variables p_1 and p_2 for convenience.

Thus, for an extended chaotic source, the two-particle correlation function $C_2(\mathsf{p}_1,\mathsf{p}_2)$ is directly related to the Fourier transform of the effective density of the source [Won94].

[4]This is often called also the Bose-Einstein correlation, because this function is based on the indistinguishability of bosons, which satisfy the Bose-Einstein statistics

2.2 The Bose-Einstein Correlation Function in Heavy-Ion Collisions

The Bose-Einstein correlation function is a useful information to probe the phase-space configuration of the source at the time of the boson emission. For example, if we could describe the effective density function $\rho_{eff}(\mathsf{r};\mathsf{p}_1\mathsf{p}_2)$ of the source by a Gaussian distribution with spatial extent R and temporal extent σ_t such that

$$\rho_{eff}(\mathsf{r};\mathsf{p}_1\mathsf{p}_2) \sim \frac{1}{R^3\sigma_t} e^{-\frac{|\vec{r}|^2}{2R^2}-\frac{t^2}{2\sigma_t^2}}, \tag{2.14}$$

its Fourier transform $\tilde{\rho}_{eff}(\mathsf{q};\mathsf{p}_1\mathsf{p}_2)$ is

$$\tilde{\rho}_{eff}(\mathsf{q};\mathsf{p}_1\mathsf{p}_2) \sim e^{-R^2|\vec{q}|^2/2-\sigma_t^2 q_0^2/2}, \tag{2.15}$$

where $\vec{q} = \vec{p}_1 - \vec{p}_2$ and $q_0 = E_1 - E_2$. From Eqs. 2.12 and 2.15, the Bose-Einstein correlation function becomes

$$C_2(\mathsf{p}_1,\mathsf{p}_2) = C_2(\mathsf{q},\mathsf{K}) = 1 + e^{-R^2|\vec{q}|^2-\sigma_t^2 q_0^2}. \tag{2.16}$$

This result for the Gaussian parameterization (Eq. 2.14) of the source can be used to analyze experimental momentum correlation data. In general, the parameters $\vec{r}$ and t are functions of p_1 and p_2. Only in special cases they can be independent of p_1 and p_2. For example, when the distribution function $S(\mathsf{p},\mathsf{r})$ is factorizable as the product of a function of p and a function of r, then the effective density and its parameters are independent of p_1 and p_2, and the effective density is identical to the space-time density distribution of the source points. This occurs when the momentum distribution of the produced bosons is independent of the location of the source points. Therefore, a Gaussian parameterization with momentum-independent parameters may be a good description for *a static source*.

However, it is clearly inadequate for a source, where the momentum distribution changes from position to position, in the inside-outside cascade description of particle production or in case of collective expansion. In the general cases, when the momentum spectrum of the produced particles depends on source coordinates, the parameters which characterize the density function $\rho_{eff}(\mathsf{r},\mathsf{p}_1\mathsf{p}_2)$ will depend on the region of p_1 and p_2 covered in the measurement.

As a consequence, the spatial region for two particles with a small momentum difference can be bounded and selected as where the gradient of expansion velocity is

small enough. For an expanding emitting source the HBT analysis cannot provide a total space-time configuration, but only a differential configuration for the selected expanding region, which can be chosen by the rapidity and the transverse momentum. Thus the spatial and temporal deviations or radii and emissions duration can only be interpreted over limited "regions of homogeneity" where the source appears stationary and position-momentum correlations are negligible [Mak88].

For the real particles, whose energy and momentum correlate according to $E^2 = m^2 + p^2$, the so-called *on mass shell constraint* should be satisfied [Yua96] as $\mathsf{q} \cdot \mathsf{K} = 0$, where $\mathsf{q} = (\vec{q}, iq_0)$ and $\mathsf{K} = (\vec{K}, iK_0)$. Therefore, we get :

$$q_0 K_0 = \vec{q} \cdot \vec{K} \tag{2.17}$$

$$q_0 = \frac{\vec{K}}{K_0} \cdot \vec{q} \equiv \vec{\beta} \cdot \vec{q}, \tag{2.18}$$

where $\vec{\beta}$ is defined as a *pair-velocity*.
The Fourier transform in Eq. 2.13 does not have a unique inverse since the four components of q are not independent[5] in respect to Eq. 2.17. In practice, the analysis of HBT correlation data must, therefore, be based on a comparison with specific models for the emission function $S(\mathsf{r}, \mathsf{K})$.

2.2.1 Space-Time Parameterizations of the Correlation Function

1-Dimensional Parameterization

The spatial-temporal information is contained in the width of the correlation function, and this must be quantified in some manner. The simplest parameterization for the correlation function is that of the single Lorentz-invariant Q_{inv} :

$$C_2(Q_{inv}) = 1 + \lambda e^{-Q_{inv}^2 R_{inv}^2} \tag{2.20}$$

[5]With this *on-shell constraint* and a factorizable source function as $S(\mathsf{r}, \mathsf{K}) = f(\mathsf{K})\rho(\mathsf{r})$, the Eq. 2.13 becomes an explicite function of $\vec{q}$ and $\vec{\beta}$(or $\vec{K}$) as

$$C_2(\mathsf{q}, \mathsf{K}) \cong 1 + \frac{|\int \mathrm{d}\mathsf{r}\rho(\mathsf{r}) e^{i\vec{q}\cdot(\vec{r}-\vec{\beta}t)}|^2}{|\int \mathrm{d}\mathsf{r}\rho(\mathsf{r})|^2}. \tag{2.19}$$

where $Q_{inv} = \sqrt{\mathsf{q} \cdot \mathsf{q}} = \sqrt{(\vec{p}_1 - \vec{p}_2)^2 - (E_1 - E_2)^2}$, and R_{inv} is the spatial-temporal extent. The coefficient λ introduced in Eq. 2.20 is the so-called *chaoticity* parameter. Experimentally, the need for this parameter is illustrated by the fact that the correlation function is often less[6] than the maximum theoretical value of 1 at $Q_{inv} = 0$. This correlation function interpolates between the case of a coherent source with $\lambda = 0$ and the case of a completely chaotic source with $\lambda = 1$ [Won94]. Although the chaoticity parameter was originally introduced to characterize the *chaoticity* of the source, in practice it is known that the parameter λ is not only sensitive to the effect of source coherence but also to impurity in particle species, resonance effects, momentum resolution, etc.[App97][Las97].

This parameterization has been applied to high-energy e^+e^-, pp, and $p\bar{p}$ collisions, where a value of $R_{inv} \sim$ 1fm was found [Act91] [Bre85] [Bre87]. However, R_{inv} is not straightforward to interpret, since Q_{inv} convolutes spatial and temporal information in a non-trivial way. Nevertheless, this parameterization is useful to analyze rarely produced particle species, such as kaons and anti-protons because of its availability with small datasets. In [Aki93] a transformation from R_{inv} to the spatial extension R is suggested in order to compare the radii of kaons to those of pions. In this thesis the same procedure is successfully carried out.

Model-independent Parameterization

As an important tool for searching "reasonable" model sources, model-independent expressions for the HBT parameters are suggested in [Cha95a] [Cha95b] and [Her95], which allow to calculate the characteristic parameters of the two-particle correlation function C_2 from an arbitrary emission function S by simple quadrature. Experimentally, these HBT parameters are obtained via a multidimensional Gaussian fit to $C_2(\mathsf{q}, \mathsf{K})$ in momentum space. To compute the Gaussian parameters of the (momentum) correlation function C_2, it is sufficient to use the Gaussian approximation[7] of the (space-time) emission function [Wie96] [Yua96],

$$S(\mathsf{r}, \mathsf{K}) \approx S(\bar{\mathsf{r}}(\mathsf{K}), \mathsf{K}) exp\Big[-\frac{1}{2} \tilde{\mathsf{r}}^{\mu}(\mathsf{K}) \mathbf{B}_{\mu\nu}(\mathsf{K}) \tilde{\mathsf{r}}^{\nu}(\mathsf{K}) \Big]. \tag{2.21}$$

Here, $\tilde{\mathsf{r}}^{\mu}$ denote the space-time coordinates relative to the effective "source center"

[6] see Fig.5.4

[7] saddle point approximation

$\bar{\mathsf{r}}(\mathsf{K})$ for a particle pair with momentum K,

$$\tilde{\mathsf{r}}^{\mu}(\mathsf{K}) = \mathsf{r}^{\mu} - \bar{\mathsf{r}}^{\mu}(\mathsf{K}), \qquad \bar{\mathsf{r}}^{\mu}(\mathsf{K}) = \langle \mathsf{r}^{\mu} \rangle, \tag{2.22}$$

while

$$(\mathbf{B}^{-1})_{\mu\nu}(\mathsf{K}) = \langle \tilde{\mathsf{r}}_{\mu} \tilde{\mathsf{r}}_{\nu} \rangle = \langle \mathsf{r}_{\mu} \mathsf{r}_{\nu} \rangle - \langle \mathsf{r}_{\mu} \rangle \langle \mathsf{r}_{\nu} \rangle \tag{2.23}$$

is the inverse of the Gaussian curvature tensor in Eq. 2.21, adjusted such that the first term in Eq. 2.21 reproduces the RMS of the full source $S(\mathsf{r}, \mathsf{K})$. The K-dependent expectation values in these definitions are defined as space-time averages over the emission function :

$$\langle f(\mathsf{r}) \rangle = \frac{\int \mathrm{d}\mathsf{r} f(\mathsf{r}) S(\mathsf{r}, \mathsf{K})}{\int \mathrm{d}\mathsf{r} S(\mathsf{r}, \mathsf{K})}. \tag{2.24}$$

Then the two-particle correlation function $C_2(\mathsf{q}, \mathsf{K})$ can be calculated analytically from Eq. 2.13 :

$$C_2(\mathsf{q}, \mathsf{K}) = 1 + \lambda exp[-\mathsf{q}^{\mu} \mathsf{q}^{\nu} \langle \tilde{\mathsf{r}}_{\mu} \tilde{\mathsf{r}}_{\nu} \rangle (\mathsf{K})]. \tag{2.25}$$

It is fully determined by the K-dependent second space-time moments $(\mathbf{B}^{-1})_{\mu\nu}$ of the source (the "effective widths" $\langle \tilde{\mathsf{r}}_{\mu} \tilde{\mathsf{r}}_{\nu} \rangle (\mathsf{K})$ or "length of homogeneity").

The Pratt-Bertsch Parameterization

In general, a Gaussian parameterization of $C_2(\mathsf{q}, \mathsf{K})$ is specified by selecting a particular choice of three independent components of the relative momentum q and implementing the on-shell constraint $\mathsf{q} \cdot \mathsf{K} = 0$ to Eq. 2.25. This is usually done in a Cartesian coordinate system with z along the beam axis and $\vec{K}$ lying in the $x - z$-plane (Fig. 2.2). One labels the z-component of the spatial 3-vector by l (for *longitudinal*), the x-component by o (for *outward*) and the y-component by s (for *sideward*). From Eq. 2.17 we then get

$$q_0 = \beta_{\perp} q_o + \beta_l q_l, \tag{2.26}$$

where $\beta_{\perp} = |\vec{K}_{\perp}|/K_0$ denotes the velocity of the particle pair transverse to the beam direction and β_l its longitudinal components.

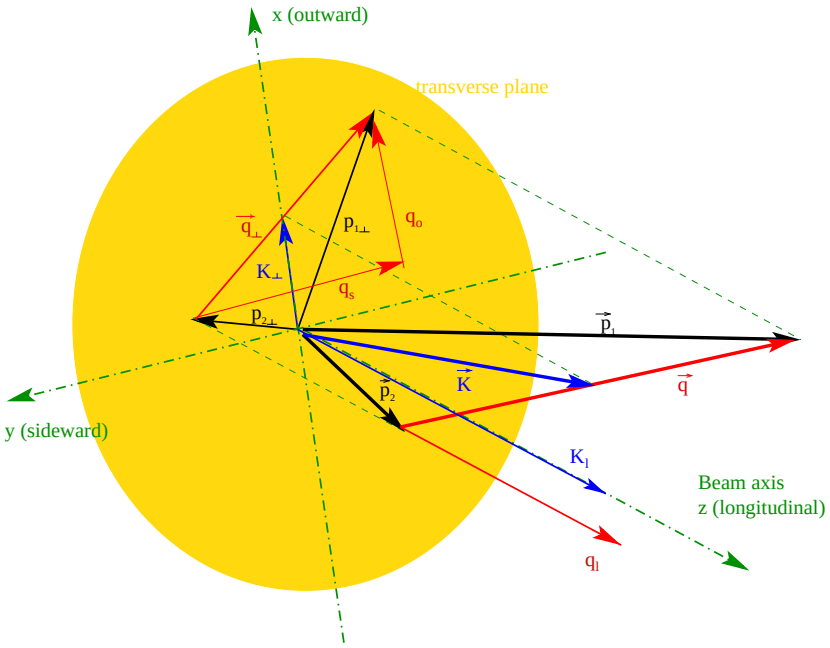

Fig. 2.2: The Pratt-Bertsch coordinate system

Using Eq. 2.26 in order to eliminate q_0 in Eq. 2.25, the standard Cartesian parameterization [Cha95a] [Cha95b] of the correlation function is obtained as :

$$C_2(\mathsf{q},\mathsf{K}) = 1 + \lambda exp\left[-\sum_{i,j=s,o,l} R^2_{ij}(\mathsf{K})\mathsf{q}_i\mathsf{q}_j\right],$$
$$R^2_{ij}(\mathsf{K}) = \langle(\tilde{\mathsf{r}}_i - \beta_i\tilde{t})(\tilde{\mathsf{r}}_j - \beta_j\tilde{t})\rangle, \qquad i,j = s,o,l \tag{2.27}$$

For an azimuthally symmetrical collision region [Cha95a] [Cha95b] [Yua96], $C_2(\mathsf{q},\mathsf{K})$ is symmetrical with respect to $q_s \to -q_s$. Then $R^2_{os} = R^2_{sl} = 0$ and

$$C_2(\mathsf{q},\mathsf{K}) = 1 + \lambda exp[-R^2_s q^2_s - R^2_o q^2_o - R^2_l q^2_l - 2R^2_{ol} q_o q_l], \tag{2.28}$$

with

$$R^2_s(\mathsf{K}) = \langle\tilde{y}^2\rangle \tag{2.29a}$$
$$R^2_o(\mathsf{K}) = \langle(\tilde{x} - \beta_\perp\tilde{t})^2\rangle \tag{2.29b}$$
$$R^2_l(\mathsf{K}) = \langle(\tilde{z} - \beta_l\tilde{t})^2\rangle \tag{2.29c}$$
$$R^2_{ol}(\mathsf{K}) = \langle(\tilde{x} - \beta_\perp\tilde{t})(\tilde{z} - \beta_l\tilde{t})\rangle. \tag{2.29d}$$

Since all components (q_s,q_o and q_l) in Eq. 2.28 are independent, this parameterization has the practical advantage which allows to analyze a small particle dataset, even

though the interpretation of these Pratt-Bertsch(BP) parameters is not simple due to the spatial-temporal mixed terms.

The Yano- Koonin-Podgoretskii Parameterization

Eliminating the redundant component of q in Eq. 2.25 as

$$q_o = \frac{1}{\beta_\perp} q_0 - \frac{\beta_l}{\beta_\perp} q_\parallel \tag{2.30}$$

$$q_\perp^2 = q_o^2 + q_s^2, \tag{2.31}$$

in the above defined coordinate system, we alternatively get the Yano-Koonin-Podgoretskii parameterization [Yan78] [Pod83] [Yua96] of $C_2(\mathsf{q},\mathsf{K})$:

$$C_2(\mathsf{q},\mathsf{K}) = 1 + \lambda exp\Big[-R_\perp^2 q_\perp^2 - R_\parallel^2 (q_\parallel^2 - q_0^2) - (R_0^2 + R_\parallel^2)(\mathsf{q}\cdot\mathsf{U})^2\Big], \tag{2.32}$$

where $\mathsf{U}(\mathsf{K})$ is a (K-dependent) four-velocity having only a longitudinal spatial component :

$$\mathsf{U}(\mathsf{K}) = \gamma_{YK}(\mathsf{K})(1,0,0,v_{YK}(\mathsf{K})), \qquad \text{with} \qquad \gamma_{YK} = \frac{1}{\sqrt{1-v_{YK}^2}} \tag{2.33}$$

and[8]

$$R_\perp^2 = \langle \tilde{y}^2 \rangle, \tag{2.34a}$$

$$R_\parallel^2 = \left\langle (\tilde{z} - \frac{\beta_l}{\beta_\perp}\tilde{x})^2 \right\rangle - \frac{\beta_l^2}{\beta_\perp^2}\langle \tilde{y}^2 \rangle \approx \langle \tilde{z}^2 \rangle, \tag{2.34b}$$

$$R_0^2 = \left\langle (\tilde{t} - \frac{1}{\beta_\perp}\tilde{x})^2 \right\rangle - \frac{1}{\beta_\perp^2}\langle \tilde{y}^2 \rangle \approx \langle \tilde{t}^2 \rangle. \tag{2.34c}$$

This Yano-Koonin-Podgoretskii(YKP)-parameterization[9] allows us to get direct information about the spatial and temporal configurations at the freeze-out time of particles, whereas the Pratt-Bertsch(BP)-parameterization in Eq. 2.29 contains in general the higher order terms with spatial and temporal informations. However, in

[8] The approximations in Eqs. 2.34 are discussed in [Wu98].

[9] The most frequently used equivalent form of Eq. 2.32 is

$$C_2(\mathsf{q},\mathsf{K}) = 1 + \lambda exp\Big[-R_\perp^2 q_\perp^2 - \gamma_{YK}^2 (q_\parallel - v_{YK} q_0)^2 R_\parallel^2 - \gamma_{YK}^2 (q_0 - v_{YK} q_\parallel)^2 R_0^2\Big], \tag{2.35}$$

practice applying it to small particle datasets may be inadequate since q_0 cannot be larger than $q_\perp$ or $q_\parallel$ due to the on-shell constraint

$$\begin{aligned} q_0 &= \vec{\beta} \cdot \vec{q} \\ &= \vec{\beta}_\perp \cdot \vec{q}_\perp + \beta_l q_\parallel . \end{aligned} \tag{2.36}$$

Additionally this parameterization has the advantage that the YKP parameters $R^2_\perp(\mathsf{K})$, $R^2_0(\mathsf{K})$, and $R^2_\parallel(\mathsf{K})$ are independent of the longitudinal velocity of the observer system in which the correlation is measured; they are invariant under longitudinal boosts [Cha95a].

2.2.2 The Expanding Source System

In nucleus-nucleus collision, there exists a very hot and dense zone of nuclear matter (*the fireball*), which is expanding in longitudinal direction. Here, every source element has its own velocity, which is dependent on its location and time of the expansion :

$$v_l = z/t. \tag{2.37}$$

In the Bjorken scenario [Bjo83] the correlation between the position of emission and the momentum of the particles is maximum, so that it becomes governed only by the temperature distribution. A consequence of relation Eq. 2.37 is the fact that the source behaves spatially and temporally in the same way in every comoving Lorentz system (*boost invariance*). This situation is comparable with Hubble expansion of the universe, where the velocity gradient $\mathrm{d}v/\mathrm{d}z = 1/t$ is equivalent to the Hubble constant.

An interesting question now is which result a HBT analysis delivers for the length of homogeneity R_z in the case of a boost-invariant and longitudinally expanding source.

The velocity gradient at the freeze-out time τ_f of the particle is given by Eq. 2.37 as

$$\frac{\mathrm{d}v_l}{\mathrm{d}z} = \frac{1}{\tau_f} \tag{2.38}$$

The measured homogeneity length should be equivalent to $\mathrm{d}z$ if the velocity difference can be compensated by the thermal velocity $\bar{v}_{therm}$. The mean thermal velocity

in one dimension can be written as :

$$\bar{v}_{therm} = \sqrt{\frac{T}{m}}, \tag{2.39}$$

where T is the freeze-out temperature. For high temperature the relativistic mass can be replaced with the transversal mass as $m_\perp \equiv \sqrt{m_0^2 + p_{therm}^2}$. From Eq. 2.38 one gets :

$$\mathrm{d}z \equiv R_z = \tau_f \sqrt{\frac{T}{m_\perp}}. \tag{2.40}$$

This equation is suggested by A. Makhlin and Y. Sinyukov in [Mak88] [Sin89]. The measured homogeneity length does not represent the geometrical extension of total source, but it contains an information about the freeze-out time τ_f of the source and depends on the transversal mass $m_\perp$ of the particle pair. The dependency of the homogeneity length on the transversal mass can be, therefore, an indication for an expansion of the source.

2.2.3 Reference Frames

Concerning the moving source, several reference frames, with their own advantages and disadvantages, can be considered for data analysis :

- **CMS (center-of-mass system)** : The center-of-mass frame of the fireball, which moves relative to the laboratory frame with the midrapidity of the system ($Y_{CM} = 2.9$) in the beam direction. It is the same for all particle pairs.
- **LCMS (longitudinally co-moving system)** : A particle-pair dependent frame, specified by $\beta_l = y = 0$, which moves relative to laboratory frame with the pair rapidity in the beam direction. In this frame, only the transverse velocity component of the particle pair is non-vanishing. It is differently defined for each particle pair.
- **FLCMS (fixed local center-of-mass system)** : A local center-of-mass frame, specified by the mean rapidity, in which the particles are distributed. The mean rapidity is calculated within the source rapidity range. It is a unique

frame for all particle pairs and it combines the advantages of CMS and LCMS frame; on one hand it is the same for all pairs like the CMS frame, simplifying the interpretation of measured quantities, and on the other hand the mean longitudinal pair momentum vanishes in the selected rapidity range, which can be chosen narrow enough to be approximated as homogeneous[10].

In this thesis, as usual in HBT analysis the FLCMS frame is used for the central rapidity region of pions and kaons.

2.3 Motivation of Kaon versus Pion Interferometry

Since the development of particle interferometry in mid-1950s, the technique of Bose-Einstein correlation analysis has been extensively used to study the source size for particles emitted from various reactions. It used to be most frequently applied to pions, which are dominantly emitted in the nuclear collisions.
One of the striking signatures of the formation of a quark-gluon plasma in nuclear collisions is an unusually long decoupling time of pions [Pra86] [Ber88]. This prediction follows simply from the second law of thermodynamics together with the expected large ratio of entropy densities in the plasma and hadronic states.
Experimentally, the pion interferometry data of NA35 [Hum88] can be explained by the hydrodynamic calculations [Ber88] for O+Au with the unusually long decoupling proper time $\tau \approx 9$ fm/c and $R_\perp \approx 3.3$ fm with an assumption of the presence of quark-gluon plasma (Fig. 2.3(b)). At the same time, however, the freeze-out geometry of the Lund resonance gas model [And87], with $\tau \approx 4$ fm/c and $R_\perp \approx 4$ fm, was also consistent with the data within experimental uncertainties (Fig. 2.3(a)).
The accidental coincidence of the two different model predictions can be interpreted by the effect of long-lived resonances. Even though the resonances freeze out at a significantly earlier time in the Lund gas model, they need an additional time to propagate before they decay into the final pions. Since the Bose-Einstein interference pattern is only sensitive to the final pion interaction coordinates [Gyu89], the effective pion freeze-out geometry is significantly larger than the resonance one, assuming

[10] see page 21

that a large fraction of the final pion multiplicity comes from the decay of long lived resonances. In fact, the Lund model [And87] predicts that a significant fraction of the negative pion multiplicity comes from the decay of long lived ω ($f_\omega \approx 0.16$) and K^* ($f_{K^*} \approx 0.09$). This fraction just happens to lead to approximately the same pion correlation function as the plasma model does.

In contrast, the kaon interferometry is quite differently predicted by the both models due to an entirely different set of hadronic resonance decays to kaons than to pions. In particular, long lived ω, η, and η' do not contribute to the kaon multiplicity. The Lund hadronic gas model predicts that roughly one half of the kaons are produced directly from string decay and the other half from the decay of K^*. Therefore, the freeze-out geometry of kaons is expected to be quite different from that of pions in the Lund gas model, i.e. the kaon proper freeze-out time should be significantly shorter than that of the pion if resonance dynamics is taken into account in the Lund gas model, while in the plasma model of [Ber88] the freeze-out geometry of all hadrons is expected to be about the same and controlled mainly by the slowness of the plasma deflagration process.

In Fig. 2.3 (c) and (d) the two different theoretical predictions of kaon interferometry in the central rapidity region ($|Y - Y_{CM}| < \frac{1}{2}$) for the reaction of O+Au at 200 AGeV are illustrated, which are calculated with the same parameters (τ and $R_\perp$) in each model as the used parameters in (a) and (b), respectively. Figures 2.3(a) and 2.3(c) compare the pion and the kaon interferometry according to the Lund resonance gas model, showing considerably different freeze-out configurations for the pion and kaon. Figures 2.3(b) and 2.3(d) shows, however, quite similar configurations for both particles in the considered kinematic cuts, assuming the quark-gluon plasma hydrodynamic model.

Therefore, the kaon interferometry can serve as a valuable complementary probe of the space-time geometry of nuclear collisions. Being less sensitive to the effects of long lived resonances than pions, a clearer distinction between the formation of long lived quark-gluon plasma droplets and more conventional resonance dynamics is possible to achieve, even though the disadvantage of kaon interferometry is, of course, the need for vastly higher statistics [$(\pi/K)^2 \sim 100$].

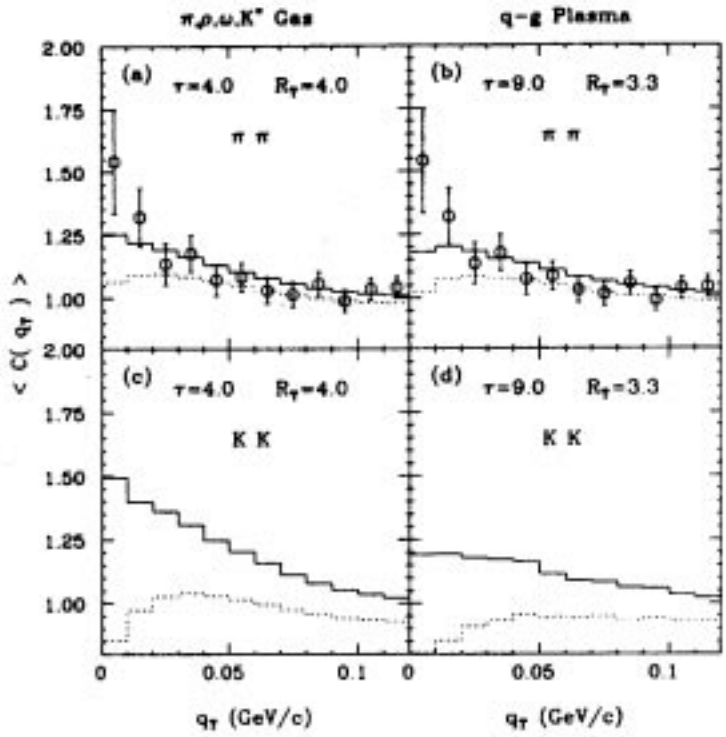

Fig. 2.3: (a),(b) Pion and (c),(d) kaon projected correlation functions vs transverse momentum difference q_T in the central rapidity region with $q_L \leq 0.1GeV$. Solid(dashed) lines indicate correlations with(without) Coulomb distortions. (a),(c) and (b),(d) correspond to predictions based on the Lund model [And87] and the plasma hydrodynamical model [Ber88], respectively. The pion data are from [Hum88].(From [Gyu90])

Chapter 3

The NA49 Experiment

The NA49 experiment is located in the North Area of the CERN (European Laboratory for Particle Physics) in Geneva. It uses a SPS (SuperProtonSynchrotron) beam line which is capable of delivering both protons and ions to the experimental area at various energies (up to 158 AGeV for Pb ions and 450 GeV for protons). NA49 was designed according to the suggestion of calculations that central Pb+Pb collisions would create conditions at or near the threshold of QGP formation [Afa99].
Since the first data taking in 1994 about 100 physicists from 10 countries are presently participating in the NA49 collaboration (see Table 3.1).

3.1 Layout of the NA49 Experiment

As illustrated in Fig. 3.1, the NA49 experimental apparatus mainly consists of two superconducting Vertex magnets, two Vertex TPCs (Time Projection Chambers) in the magnets, two "main" TPCs behind the magnets and four TOF (Time-Of-Flight) walls on both sides of the beam.
Particle identification (PID) requires the complete determination of a particle's four-momentum. The TPCs (VTPC1/2 and MTPC-R/L) enable one to determine the spatial components of the momentum by measuring the curvature of a charged particle's trajectory in a given magnetic field. To complete the PID, a further measurement of the mass, energy, or velocity, is required. Since tracking chambers work by

Department of Physics, Univ. of Athens	Athens, Greece
Lawrence Berkeley National Laboratory, Univ. of California	Berkeley, USA
Birmingham University	Birmingham, England
Research Institute for Particle and Nuclear Physics	Budapest, Hungary
Gesellschaft für Schwerionenforschung	Darmstadt, Germany
University of California at Davis	Davis, USA
Joint Institute for Nuclear Research	Dubna, Russia
Fachbereich Physik der Universität Frankfurt	Frankfurt, Germany
CERN	Genf, Switzerland
University of Houston	Houston, USA
Kent State University	Kent, USA
Institute of Nuclear Physics	Krakow, Poland
University of California at Los Angeles	Los Angeles, USA
Fachbereich Physik der Universität Marburg	Marburg, Germany
Max-Planck-Institut für Physik	München, Germany
Yale University	New Haven, USA
Institute of Physics	Bratislava, Slovakia
Nuclear Physics Laboratory, Univ. of Washington	Seattle, USA
Institute for Nuclear Studies	Warsaw, Poland
Institute for Experimental Physics, Univ. of Warzaw	Warsaw, Poland
Rudjer Boskovic Institute	Zagreb, Croatia

Table 3.1: The NA49 Collaboration (September 1999)

collecting the ionization of a charged particle, this can be performed by measuring the specific energy loss $\mathrm{d}E/\mathrm{d}x$ of a particle. However, in fixed target experiments, most of the produced particles are highly relativistic (i.e. $\beta\gamma \gg 1$). In such a case, the specific energy loss is a weak function of velocity (Fig. 3.2) and thus the contamination by undesired particle species is rather high, because the energy loss curves are not clearly separable. For example, the kaon identification with low contamination, which are particularly much less abundant than pions and hardly separable from protons by the $\mathrm{d}E/\mathrm{d}x$-method, requires a time-of-flight (TOF) detector system, which delivers information about particle masses m by measuring the particle velocity (Eq. 4.1). Combining $\mathrm{d}E/\mathrm{d}x$ from TPCs and m^2 from TOF yields excellent PID for kaons with negligible contamination (Fig. 4.2 and 4.3).
The main components of the NA49 experiment are briefly summarized below :

- The superconducting dipole magnets offer a total bending power of up to 9 Tm over 7 m length (about 1.5 T). The magnets determine to a large extent the phase space available for tracking.
- The VTPC1 is located inside the Vertex magnets focusing on the midrapidity

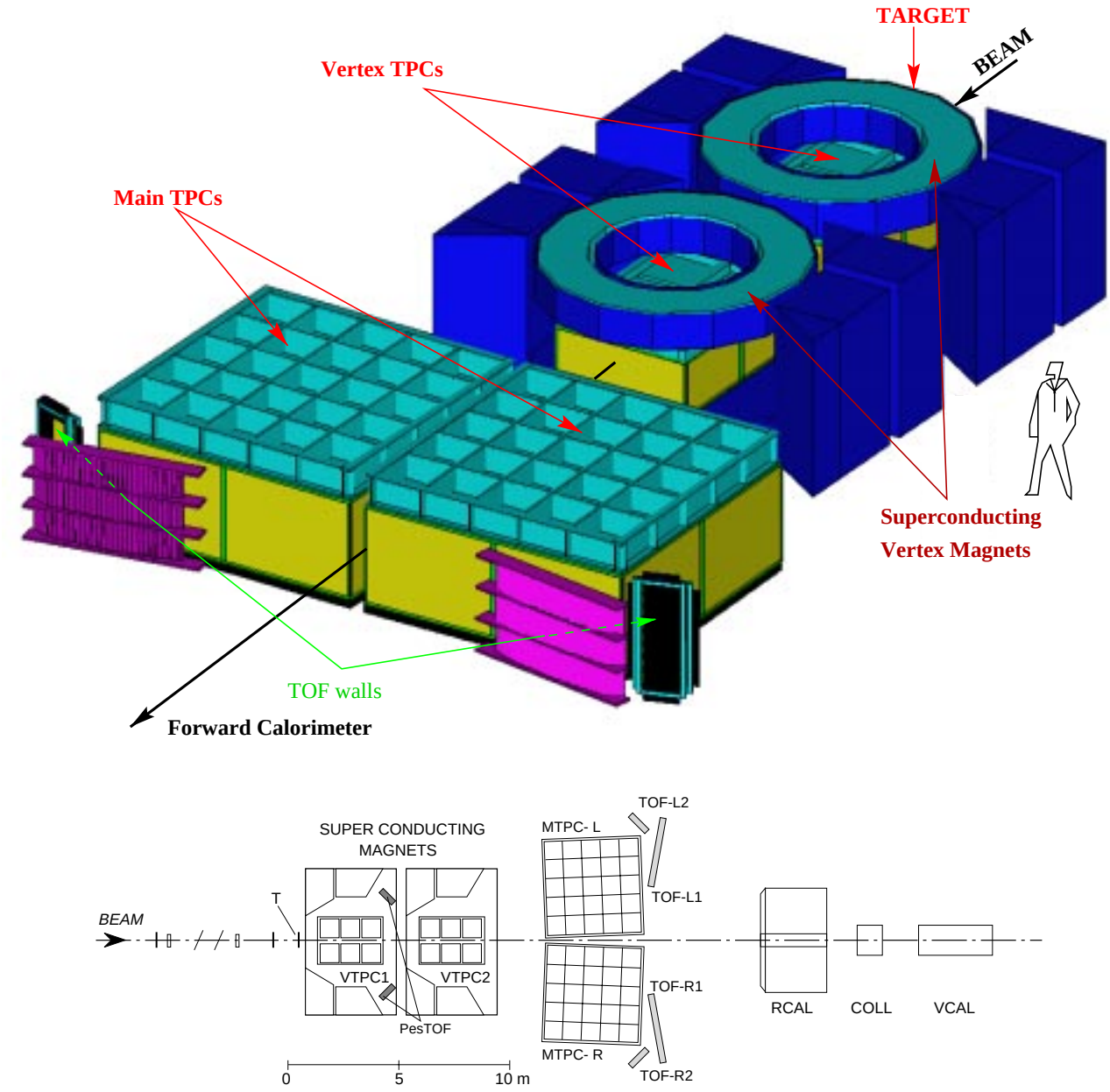

Fig. 3.1: A schematic overview of NA49 experimental apparatus showing the target T, the VTPCs within the superconducting vertex magnets, the MTPCs and the TOF walls. The ground surface is about 6x13 m^2 without the calorimeters.

pions ($y_{mid} \simeq 2.9$) in the Pb+Pb collisions at 158 AGeV. Besides VTPC1, in order to facilitate the reconstruction of neutral strange hadrons (i.e. Λ, K^0, etc.), which have a $c\tau$ of the order of centimeters to a few meters, VTPC2 is settled also inside the second Vertex magnet. Each VTPC covers the volume of 2000x2500x980 mm^3. For a large acceptance of produced particles two larger "Main" TPCs (MTPC-L/R) are installed on both sides of the beam behind the magnets, covering the volume of 3900x3900x1800 mm^3 for each MTPC.

- Two walls of "main" time-of-flight (TOF-R1/L1) pixel scintillator detectors stand behind the MTPCs. In particular their locations are adjusted to the midrapidity of kaons in the Pb+Pb collision at 158 AGeV. In order to extend TOF determination into low momentum range and into the backward hemisphere, a grid scintillator system (TOF-R2/L2) and arrays of PesTOF counters are appended as shown in Fig. 3.1.

- A ring calorimeter (RCAL) enables to measure transverse energy and a vetocalorimeter (VCAL) serves as a central trigger by measuring the forward energy in heavy-ion running.

In this thesis pions and kaons at midrapidity in central Pb+Pb collisions at 158 AGeV are investigated. For kaon identification the TOF information will be used to obtain a clean kaon sample (in Section 4.1.1). On the other hand, midrapidity pions have to be taken from VTPC1 using the dE/dx identification method (in Section 4.2.2).

3.1.1 The TPC Tracking System

The track reconstruction is performed with the measured spatial points on a track in the TPCs. TPCs have an sensitive volume containing a gas-mixture of Ar, CH_4 and CO_2. A charged particle transversing this sensitive volume produces electrons and ions through ionization processes in the medium. These electrons drift towards a readout plane under the influence of a homogeneous electric field set by the field cage. On the readout plane, a system of anode and field wires strung above a segmented cathode plane multiply the delivered electric signal in the avalanche process. The localization of this signal on the readout pad-plane (26886 channels on the plane

of 3.1 m^2 for each VTPC) provides two of three spatial coordinates of a charge of cluster (a point on a track). The third coordinate can be deduced from the drift time of the electrons by the given drift velocity.
Using the track finding algorithm, the particle tracks are reconstructed by the coordinates of these charged clusters. For matched global tracks a minimum of 8 clusters is required, a possible maximum being 234 clusters (see Fig. 4.12). It is determined by the production kinematics of tracks at the vertex, combined with the momentum dependence of magnet deflection. The detailed descriptions of VTPCs and the track reconstruction are given in [Las97]. The typical reconstructed tracks in TPCs are illustrated in Fig. 3.3.
Besides the track reconstructions, another important task of TPCs is the measurement of the specific energy loss $\mathrm{d}E/\mathrm{d}x$. The measured electrical signal is proportional to the specific energy loss of the transversing particle. The specific energy loss of a particle is obtained by integrating these signals over the full track of the particle in the sensitive volume and averaging with "truncated mean"-method [Moc97].
Since the specific energy loss of a particle in the gas depend only on the velocity of the particle, this enables to distinguish the particle species with different mass and the same momentum. The particle can be, then, identified by the measurement of

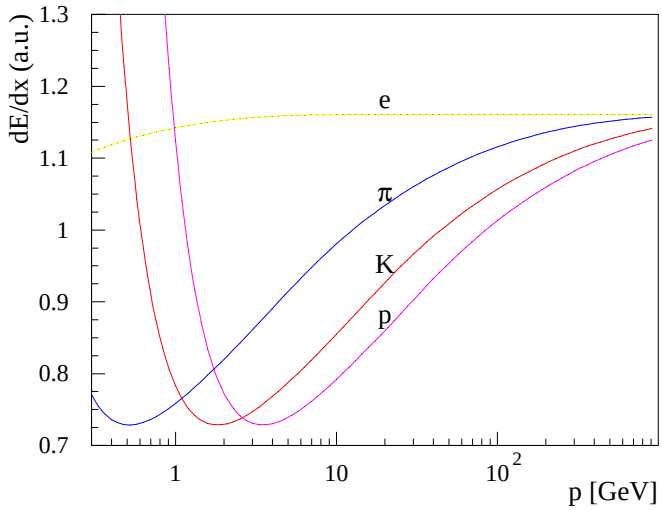

Fig. 3.2: Specific energy loss function of momentum for different particle species [Fri99]

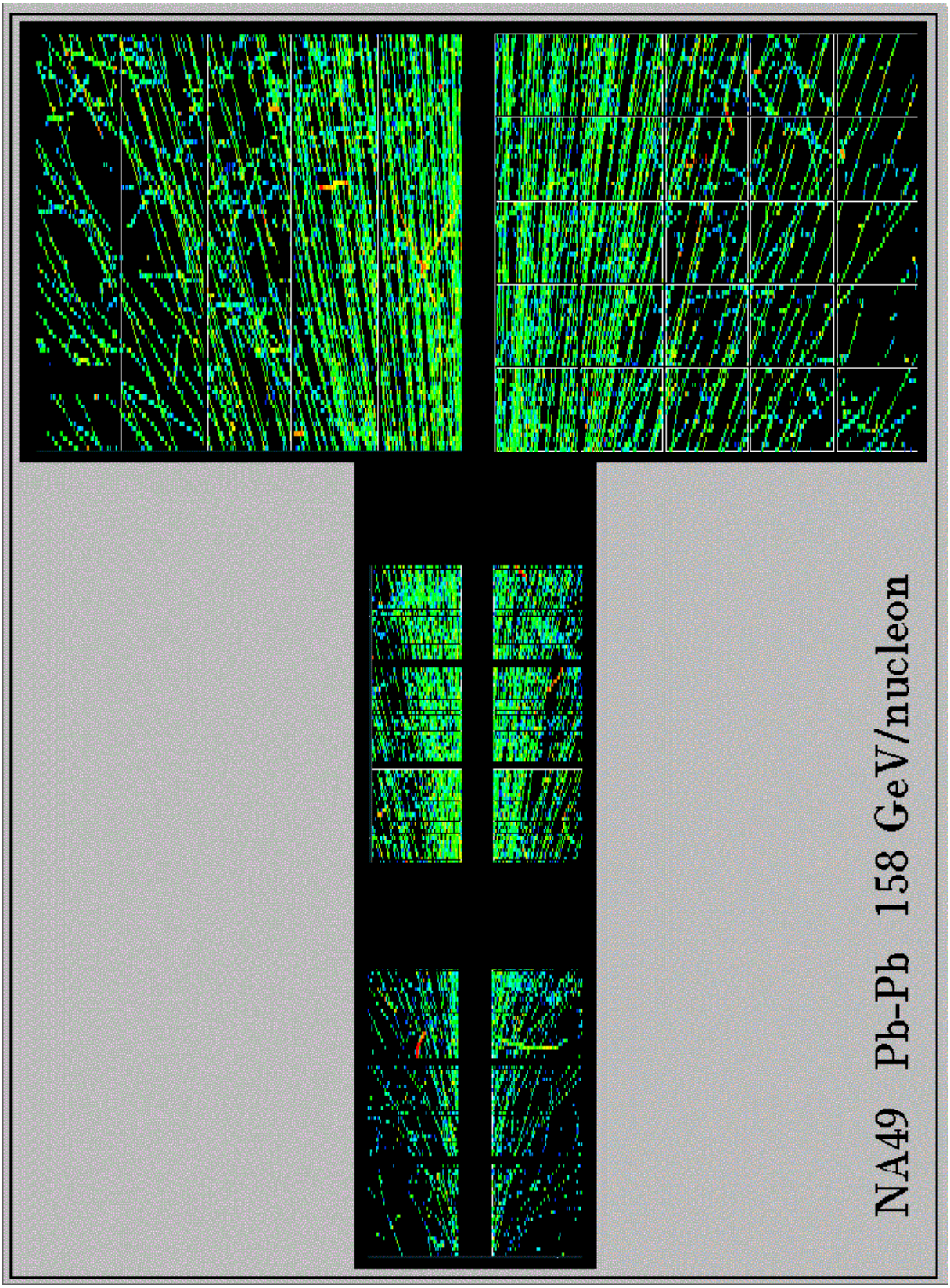

Fig. 3.3: Topview of a central Pb+Pb event as detected by the four TPCs. Only a 7mm high slice around the beam plane is depicted in order to allow for a resolution of tracks in the projection.

its dE/dx and momentum, as illustrated in Fig. 3.2.

3.1.2 Time-of-Flight System

Since particle identification by energy loss measurement alone fails at minimum ionization, and since - even with the good dE/dx resolution achieved - kaon selection on a track-by-track basis is not feasible, independent particle identifiers based on time-of-flight methods were required in the NA49 detector concept.
For the ideal complement, two TOF walls (TOF-L1 and TOF-R1 in Fig 3.1) are installed at the specific position focusing on the midrapidity region of kaon in the Pb+Pb collision at 158 AGeV. They were constructed by the Dubna group and Marburg group in the NA49, respectively, and possess 891 individual scintillation detectors on a total surface of 2.2 m^2, which were designed as rectangular scintillators glued directly to one photomultiplier per detector. The scintillators have a thickness of 23 mm matched to the photocathode diameter, a height of 34 mm and horizontal widths between 60 and 80 mm. The photomultiplier outputs are split and fed into constant-fraction discriminators followed by time-to-digital converters, and to charge-to-digital converters. This electronics system is housed in FAST-BUS and VME crates.

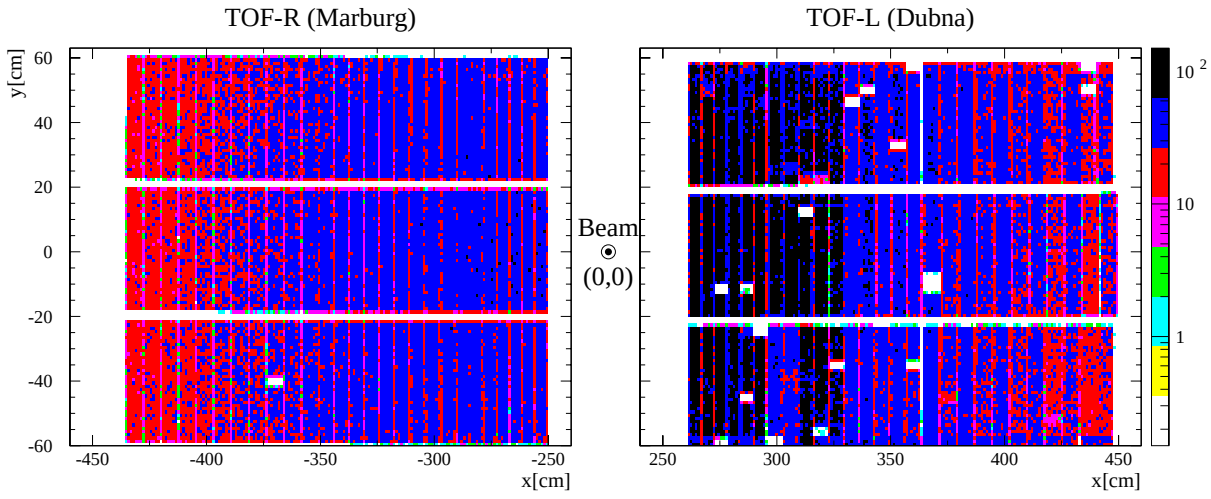

Fig. 3.4: Track hits on the TOF-walls in magnet STD+ (RUNS in 1996) and their positions with respect to the beam position at (0,0).

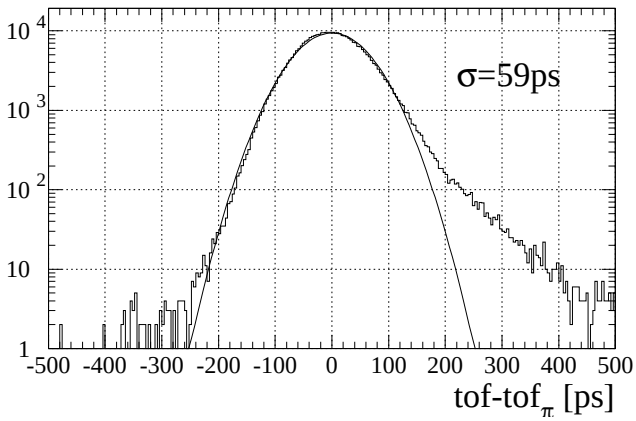

Fig. 3.5: Distribution of time difference between measured time-of-flight and time-of-flight calculated for pion (TOF-R) [Eck96]

In Fig 3.4 the responses of scintillators of TOF-R1/L1 walls are illustrated in their position plane, which is coordinated regarding the neutral beam position as the origin(0,0), upward direction as the y-axis, and leftward direction with respect to the beam direction (z-axis) as the x-axis. The overall time resolution of the TOF-R1 (Marburg) system is demonstrated in Fig. 3.5, which shows, for about 2 million tracks in 40000 central Pb+Pb events the distribution of differences between the measured time-of-flight and that predicted time-of-flight from the measured momentum assuming the pion mass. The distribution can be described by a Gaussian with a standard deviation of 60 ps. Double hits due to the finite granularity, edge effects and background from γ's are the main sources of efficiency reduction. The sum of all losses, as experimentally determined by comparison with the TPC track data, amounts to 29% on average, with a maximum of 34% in the central region closest to the Pb-beam.

For particles in the acceptance of the TOF detectors the $\mathrm{d}E/\mathrm{d}x$ information from the TPCs is available simultaneously with the time-of-flight. The combination of both methods improves the particle identification considerably. This is demonstrated in Fig. 4.2, where particles in the momentum range 4-6 GeV/c are sorted corresponding to their $\mathrm{d}E/\mathrm{d}x$ signal and the squared mass obtained from the time-of-flight and momentum measurement. Particularly the TOF measurement is needed for the distinction between kaons, protons and deuterons, whereas at momenta above approximately 4 GeV/c the separation of the lighter particles (e, π) from the group of

heavier ones (K,p,d) is performed essentially by dE/dx methods (see also Fig. 3.2).

3.2 Survey of Datasets

The main program of the NA49 Experiment is the investigation of the lead-on-lead nuclear collisions at the highest energy, 158 AGeV in SPS. In this thesis the most central collisions, which represent 5% of the total inelastic reaction cross-section (impact parameter of maximum 3.5 fm [Alb95]), were taken to gather the highest statistics of kaons.
In the beam time 1995b (November and December in 1995) about 385,000 such events were taken in the magnetic field configurations STD+ as well as STD−. The reconstruction of these events was performed in July of 1996 with a software version named 96C/E.
In order to increase the kaon statistics the TOF data of 1996 (version : 00B) were additionally taken for kaon HBT analysis, which are about 419,000 events in the configuration STD+. In the 1996 data, the same centrality selection as in 1995 was obtained by an offline cut in the energy measured by the vetocalorimeter. The list of runs is displayed together with the number of events in Tab. 3.3.
For pions the VTPC1-data of 1995 (version : 96F) were used to gather pions with midrapidity. As listed in Tab. 3.2, the five runs were enough to obtain pions because of their enormous abundance.

Run-No.	Events
95-808	5,324
95-809	10,500
95-810	10,258
95-814	6,655
95-820	10,796
Total	43,533

Table 3.2: The used run list with number of events for VTPC1

95 STD+ TOF		95 STD- TOF		96 STD+ TOF			
Run-No.	Events	Run-No.	Events	Run-No.	Events	Run-No.	Events
95-808	11,165	95-868	10,879	96-1389	11,740	96-1424	3,955
95-809	10,820	95-869	10,935	96-1391	11,671	96-1425	5,121
95-810	10,901	95-870	4,959	96-1392	5,914	96-1426	1,602
95-814	6,765	95-876	5,365	96-1393	6,617	96-1427	11,347
95-815	1,418	95-877	10,700	96-1394	12,463	96-1432	6,344
95-817	2,874	95-878	10,779	96-1395	9,682	96-1433	12,497
95-820	11,013	95-879	1,694	96-1396	1,908	96-1434	2,737
95-821	7,594	95-881	4,887	96-1397	2,200	96-1435	9,921
95-822	1,652	95-896	2,504	96-1398	11,040	96-1436	12,752
95-823	1,734	95-897	8,811	96-1399	4,353	96-1437	13,090
95-824	926	95-898	11,034	96-1400	8,894	96-1439	7,289
95-827	9,558	95-899	11,086	96-1408	4,386	96-1441	3,130
95-828	2,041	95-900	2,787	96-1409	2,332	96-1442	13,346
95-829	8,615	95-901	3,114	96-1410	2,811	96-1443	13,057
95-830	2,211	95-902	5,025	96-1412	11,895	96-1444	12,888
95-831	8,935	95-903	10,945	96-1413	12,272	96-1445	12,960
95-832	3,458	95-904	10,931	96-1416	11,532	96-1446	8,383
95-833	7,331	95-905	11,193	96-1417	12,796	96-1448	4,443
95-834	2,225	95-906	11,210	96-1418	12,636	96-1449	11,163
95-835	8,268	95-908	387	96-1419	12,593	96-1451	12,988
95-836	11,134	95-914	10,793	96-1420	12,504	96-1452	7,636
95-837	10,696	95-915	10,552	96-1421	12,243	96-1456	3,849
95-838	578	95-992	10,628	96-1422	12,174	96-1457	12,780
95-839	10,200	95-993	2,580	96-1423	3,763	96-1458	5,605
95-844	9,153	95-994	8,144				
95-845	10,911	95-995	9,766				
95-846	10,699						
Total	182,875	Total	201,688	Total	419,302		

Table 3.3: list of the runs used for kaon HBT analysis

Chapter 4

Data Selection

Before starting the HBT analysis, kaons and pions must be selected from the datasets shown in Tab. 3.2 and 3.3. The data selection includes the following processes :

1. Particle identification

   The kaons are identified by the combined informations of the mass from TOF and the $\mathrm{d}E/\mathrm{d}x$ from MTPC (section 4.1.1), while the pions are identified only by the $\mathrm{d}E/\mathrm{d}x$ from VTPC1 (section 4.2.2).

2. Phase space (rapidity and p_T) selection

   Acceptance cuts : As kaon PID is based on the TOF information and TOF is restricted to midrapidity kaons, the same rapidity region (3 $\leq$ Y $\leq$ 3.5) was used for the pion analysis. This means employing the VTPC1 data (section 4.2.1).

3. Track selection

   - TOF hits : for the signal quality the signal charge (QDC signal) and the hit position in the scintillator are restricted, and the simultaneous double hits on the same scintillator are ignored (section 4.1.3).
   - VTPC1 tracks : to remove *ghost tracks*[1] the track resolution in VTPC1 is studied and the combination of track points-cut and the distance-cut

[1] see page 55

is applied (section 4.2.3).

4. Pair cuts in the mixed-event background to account for detector constraints - TOF single hits (section 4.1.4) and VTPC1 minimal distance (section 4.2.3).

5. Event cuts : since the HBT analysis always requires at least two candidates for the Bose-Einstein signals, the events with 2 particles minimum should be selected in the mixed-event background. This event constraint effect is studied (section 4.1.5 and 4.2.4).

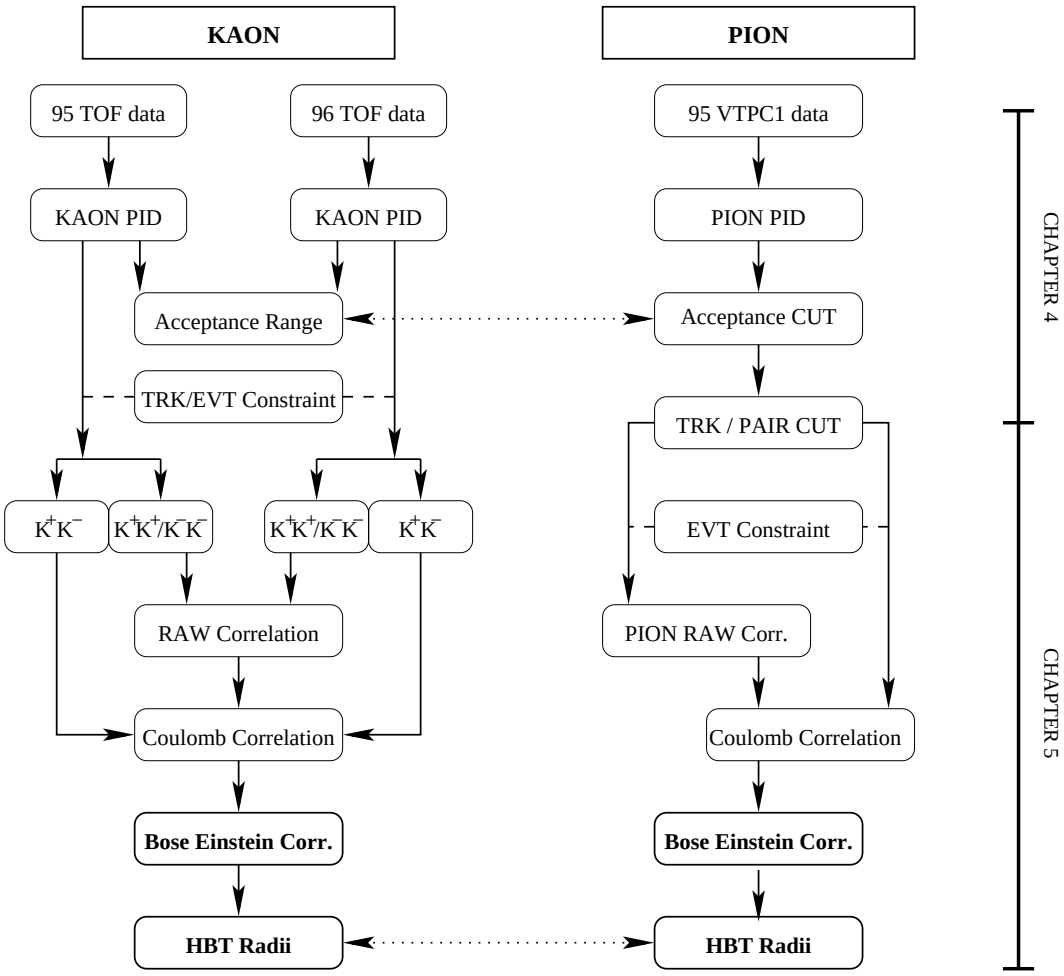

Fig. 4.1: The flow chart for HBT analyses and comparison between kaons and pion. The dashed lines indicate considerations and check points, while the dotted lines denote influence and comparison.

In order to avoid confusion and to carry out the assignment of this thesis effectively, the flow chart of all processes to be executed is illustrated in Fig. 4.1.
In the left column of Fig. 4.1, the processes for kaon HBT analysis are listed and in the right column those for pion HBT analysis. As a milestone the matching chapters are additionally listed.
Subsequently in Chapter 5 the HBT analyses for pions and kaons will be started. As it is explained in Section 5.1, the *raw* correlation between like-sign particles should be corrected by the Coulomb effect, which is extracted from the unlike-sign particle correlation.
Particularly due to the poor statistics of kaons, the weighted means of the results of the 95 data and those of the 96 data are taken for analysis. In this thesis the 1-dimensional[2] and 3-dimensional[3] HBT analyses are done only with the Yano-Koonin-Podgoretskii parameterization[4] for pions and kaons, respectively.
Finally, the interpretation and comparison of HBT radii of kaons to those of pions will be done in Section 5.2.3 for the 1-dimensional analysis and in Chapter 6 for 3-dimensional analysis, respectively.

4.1 Kaon Selection from TOF Data

As explained in the previous chapter, the $\mathrm{d}E/\mathrm{d}x$ information is not sufficient for the identification of kaons, because the specific energy losses of kaons and protons are too close to provide a clear separation. The proton contamination in the kaon sample would destroy the Bose-Einstein correlation between kaon pairs due to its Fermi-Dirac anti-correlation. The TOF information is therefore requested for a good identification of kaons in spite of the shortcoming of its limited acceptance range.

4.1.1 Particle Identification

For the identification of kaons the $\mathrm{d}E/\mathrm{d}x$ from MTPC and the m^2 from TOF can be utilized (see Fig. 4.2). The information of the time-of-flight t of a particle from

[2]see page 21
[3]see page 25
[4]see page 25

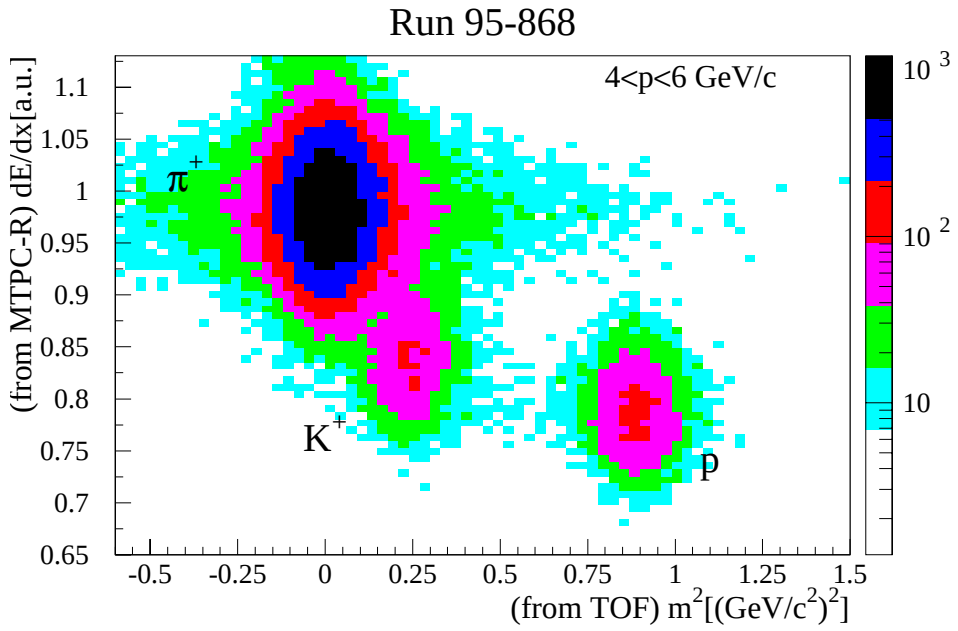

Fig. 4.2: dE/dx vs. m^2 diagram for the momentum of $4 < p < 6$ GeV/c.

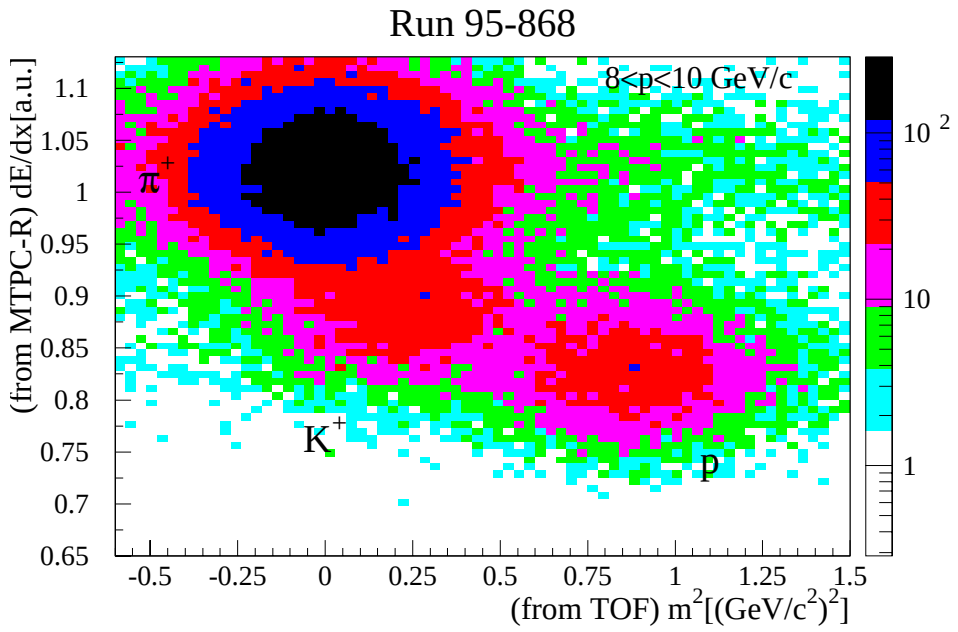

Fig. 4.3: dE/dx vs. m^2 diagram for the momentum of $8 < p < 10$ GeV/c.

the start detector (S1 near the target in Fig. 3.1) to the stop detector (TOF-R/L) and the track length s determined by the tracking system allow us to calculate the velocity $\beta = s/t$. Furthermore, with the momentum information from TPCs the squared mass can be calculated by the relation :

$$m^2 = \frac{p^2}{\beta^2\gamma^2} = \frac{p^2(1-\beta^2)}{\beta^2} \tag{4.1}$$

with the error [Eck96] of

$$\sigma_{m^2} = \sqrt{\sigma_{p^2}^2(\frac{1-\beta^2}{\beta^2})^2 + \sigma_\beta^2(\frac{2p^2}{\beta^3})^2}, \tag{4.2}$$

which yields that the error is independent of the particle mass, i.e. it should be same for all species of particles, and mainly depends on the particle momentum.
The distribution of particles in the dE/dx-m^2 plane depends not only on the mass and the specific energy loss, but also on the particle momentum, since the specific energy loss and the m^2 resolution are functions of the momentum (compare Fig. 4.2 to Fig. 4.3). The parameterization of this distribution as a function of the mass, the specific energy loss and the momentum for each particle type, i.e. π, K and p, must be carried out to define a particle selection cut and calculate its efficiency and contamination.

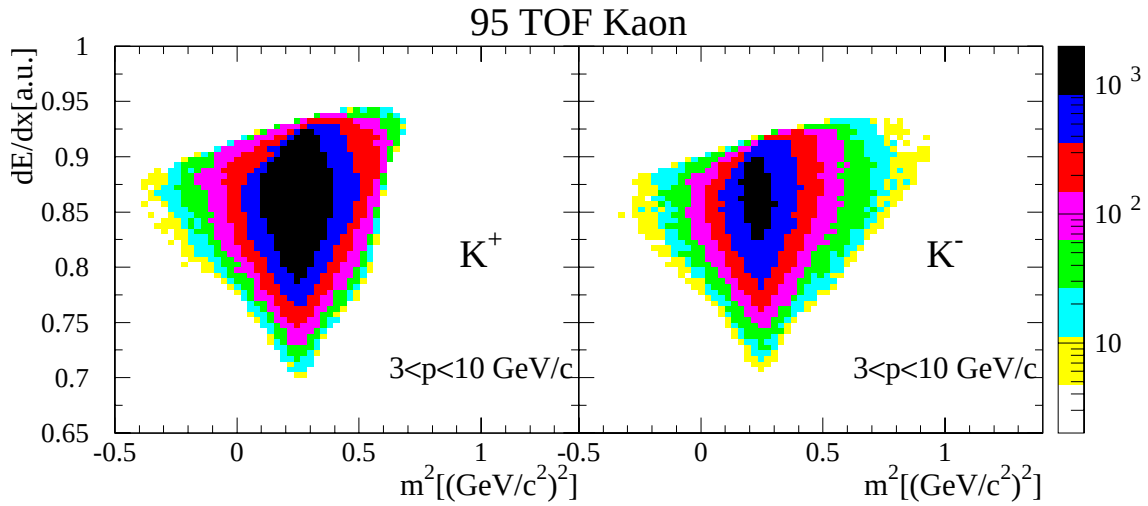

Fig. 4.4: Selected cut for charged kaons of the given momentum range in TOF-R 95 STD- and STD+

momentum	entry	K^+(%)	π^+(%)	p(%)	entry	K^-(%)	π^-(%)	$\bar{p}$(%)
$3 \leq p < 4$	12,816	97.64	2.36	0.	5,365	98.33	1.67	0.
$4 \leq p < 5$	47,972	95.59	4.41	0.	21,777	94.32	5.68	0.
$5 \leq p < 6$	95,754	93.48	6.52	0.	45,609	92.50	7.50	0.
$6 \leq p < 7$	110,572	90.72	8.95	0.33	51,293	90.33	9.64	0.03
$7 \leq p < 8$	91,054	86.92	11.38	1.70	43,047	86.83	12.56	0.61
$8 \leq p < 9$	67,737	82.44	12.68	4.88	31,006	85.32	13.02	1.66
$9 \leq p \leq 10$	45,181	78.44	13.86	7.70	20,016	84.14	13.01	2.84
total	471,086				218,113			
weighted mean		**88.86**	9.29	1.85		**89.41**	9.97	0.62

Table 4.1: Contributions to the kaon cut for the 95 TOF kaon sample

Because the mass and specific energy loss of the particle are independent measurements, the distribution function can be factorized as [Fri99] :

$$f^i(m, E, |\vec{p}|) = g^i(m, |\vec{p}|) \cdot h^i(E, |\vec{p}|) \tag{4.3}$$

where m denotes the mass of particle, E the specific energy loss, $\vec{p}$ the momentum of the particle and $i = \pi, K, p$. [5]

The parameterization of the dataset 95 TOF is performed in [Fri99] and [Hen97], and used to calculate the contamination of the kaon sample, which is defined by a graphical cut in the $\mathrm{d}E/\mathrm{d}x$-m^2 plane of the momentum range of 3 - 10 GeV with a step size of 1 GeV. The selected kaons are shown in Fig. 4.4 and the contributions of the particle species to the cut are given in Tab. 4.1.

For the dataset 96 TOF the parameterization of $g^i(m, |\vec{p}|)$ and $h^i(E, |\vec{p}|)$ in Eq. 4.3 is performed in the same way. It differs from the 1995 parameterization mainly because of the improvements in the $\mathrm{d}E/\mathrm{d}x$ resolution achieved in between. Finally, the parameterized function $f^i(m, E, |\vec{p}|)$ and the experimental data are compared and illustrated as an example for the momentum range of 5-6 GeV in Fig. 4.5. For the parameterization of $g^i(m, |\vec{p}|)$ a Gaussian plus an exponential tail was employed ; for $h^i(E, |\vec{p}|)$ only a Gaussian distribution is used.

For each momentum bin (3-10 GeV with a step size of 1 GeV) the kaon selection is performed choosing an area within 2.5 standard deviation from the kaon peak. An

[5] The electrons are excluded from the parameterization, since they are, for the most part, generated by secondary interactions in the detector and do not influence the kaon identification.

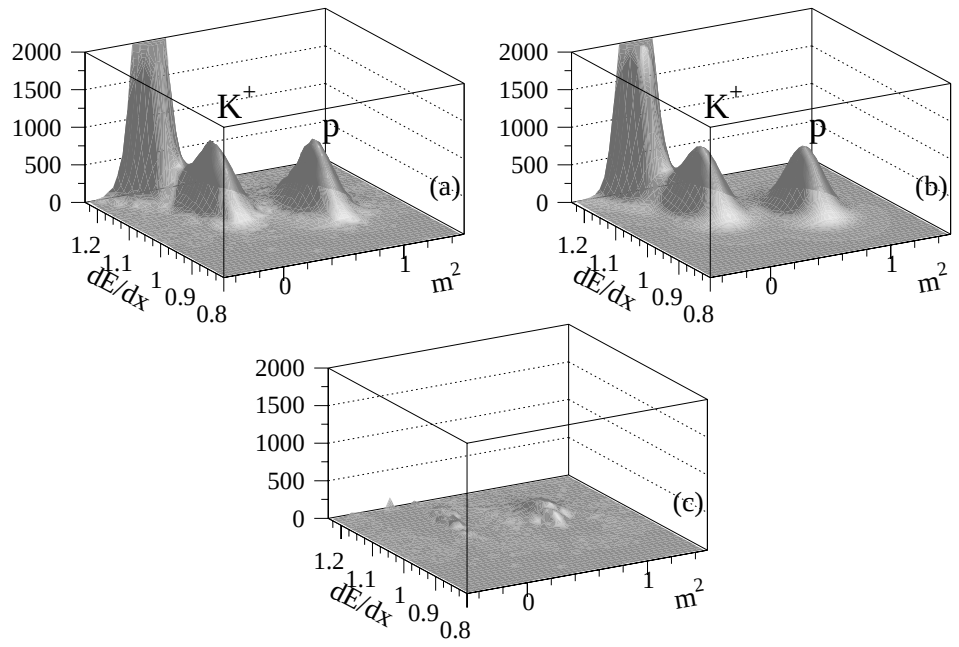

Fig. 4.5: The comparison of the experimental distribution of particle in the dE/dx-m^2 plane and the parameterized distribution function. (a) The experimental distribution from dataset 96 TOF STD+ in the momentum range of 5-6 GeV. (b) The parameterized distribution function with same variables. (c) The subtracted distribution : (c)=(a)-(b).

additional requirement is that the differential kaon contribution at each point of the selected region be at least 50 %. Fig. 4.6 shows the area defined in such a way, while Tab. 4.2 gives the contribution of the particle species.

As one can see from Tabs. 4.1 and 4.2, for low momenta the separation of kaons from pions and protons is almost perfectly done, while for higher momenta (as in Fig. 4.3) the separation power decreases. By means of the graphical cut of kaons in **95 TOF data**, the weighted mean of particle efficiency is **88.86** ($\pm$5.38) **% for K$^+$** and **89.41** ($\pm$3.71) **% for K$^-$**, respectively. Owing to the improvement of track-reconstruction software which also improves the dE/dx resolution in **96 TOF data**, the 2.5 standard deviation cut for kaons has the mean particle efficiencies of **93.32** ($\pm$6.06) **% for K$^+$** and **95.21** ($\pm$7.17) **% for K$^-$**.

The comparison of the mean kaon purity of the selection (Tabs. 4.1 and 4.2) reflects

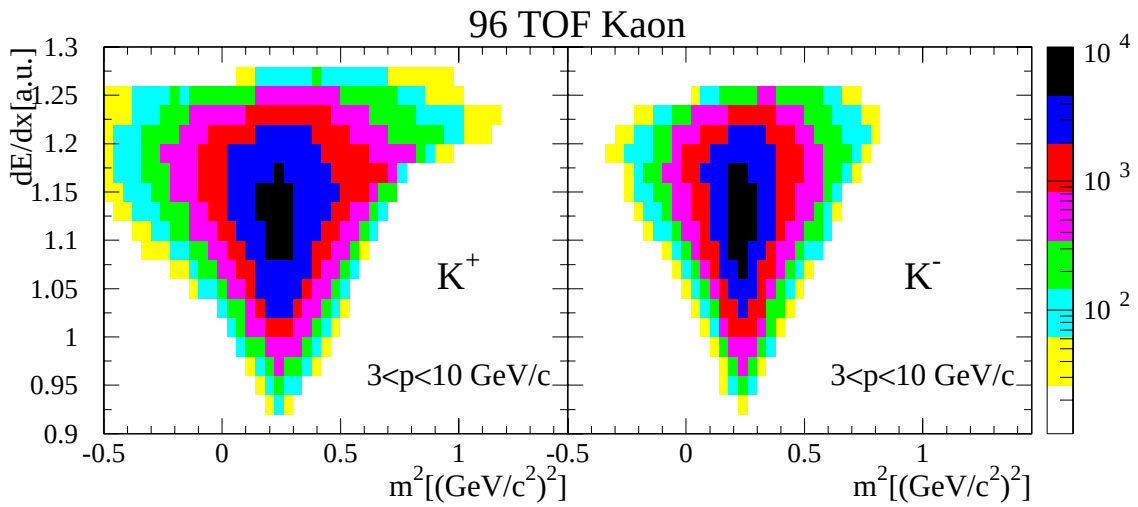

Fig. 4.6: Selected cut for charged kaons of the given momentum range in TOF 96 STD- and STD+

momentum	entry	K^+(%)	π^+(%)	p(%)	entry	K^-(%)	π^-(%)	$\bar{p}$(%)
$3 \leq p < 4$	6,678	99.79	0.21	0.	4,382	99.83	0.17	0.
$4 \leq p < 5$	25,505	98.92	1.08	0.	19,024	98.99	1.01	0.
$5 \leq p < 6$	50,901	97.00	3.00	0.	39,016	97.22	2.78	0.
$6 \leq p < 7$	64,186	95.60	4.36	0.04	48,488	95.79	4.20	0.01
$7 \leq p < 8$	62,296	93.55	5.12	1.33	44,175	94,43	5.00	0.57
$8 \leq p < 9$	54,234	89.14	5.53	5.33	32,866	92.41	4.70	2.89
$9 \leq p \leq 10$	44,046	86.35	5.56	8.09	20,804	92.73	3.82	4.45
total	307,846				208,755			
weighted mean		**93.32**	4.30	2.38		**95.21**	3.77	1.02

Table 4.2: Contributions to the 1996 TOF kaon selection

the improvements in the dE/dx resolution from 1995 to 1996.

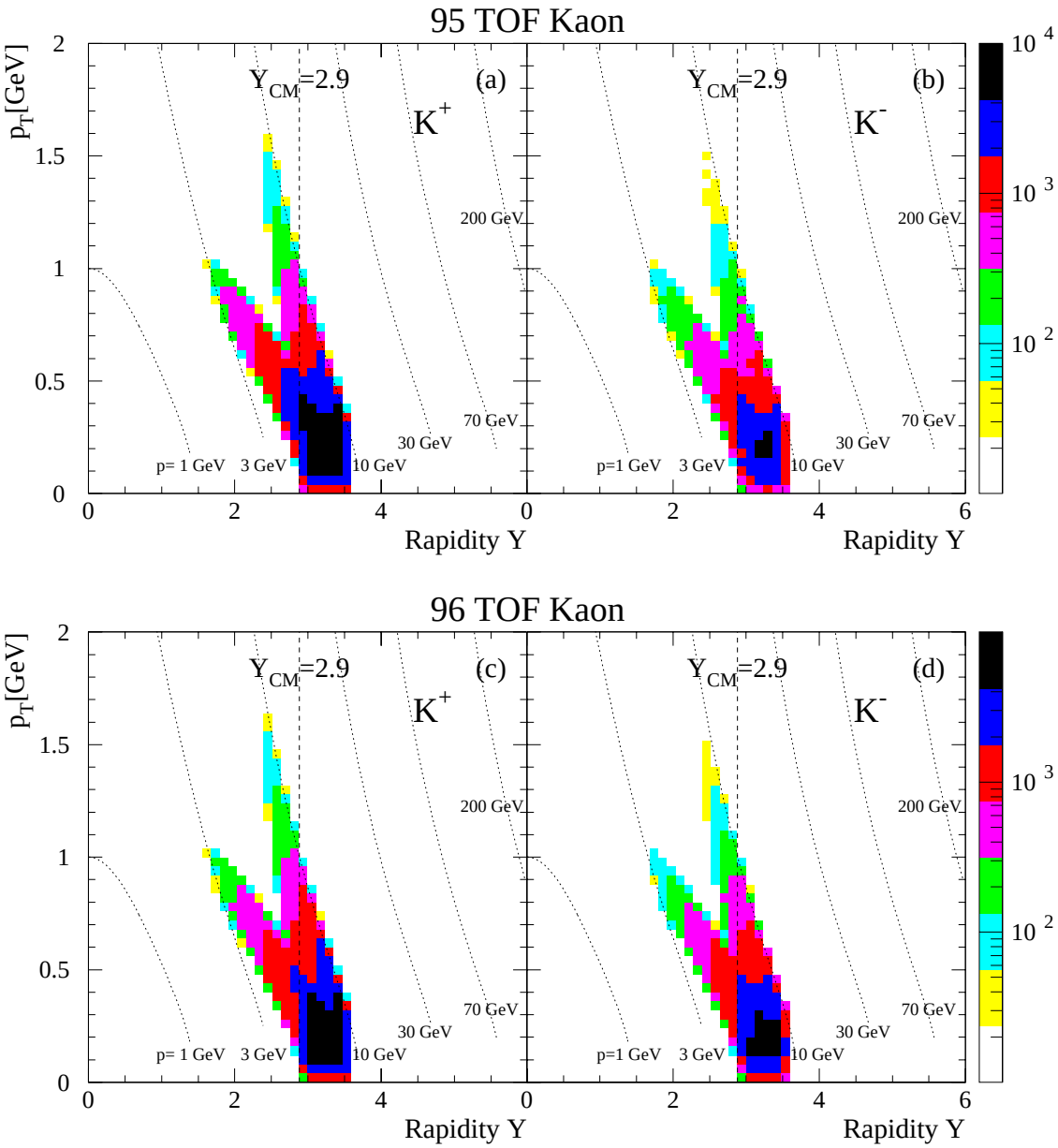

Fig. 4.7: TOF acceptance region in rapidity Y and transversal momentum p_T for kaons : (a) and (b) for 95 TOF kaons ; (c) and (d) for 96 TOF kaons. Lines of constant momenta are shown by the dotted curves according to the relation $p_T = \frac{\sqrt{p^2 - m^2 sinh^2(Y)}}{cosh(Y)}$, and the dashed line indicates the center-of-momentum rapidity Y_{CM}. In all cases the wrong side tracks (the left 'branch') are included (see text).

4.1.2 Acceptance Region for Selected Kaons

In 158 AGeV collisions, the rapidity of the produced particles is distributed[6] between 0 and 6. As discussed in chapter 3, the TOF walls cover a small range around kaon midrapidity (Fig. 4.7). The two branches in the acceptance region belong to the so-called "*right side*" and "*wrong side*" tracks, being emitted in the same/opposite hemisphere as the detecting TOF wall, respectively.
For a direct comparison of the HBT results of pions and kaons, the same rapidity region ($3 \leq Y \leq 3.5$) must be chosen for the pion sample. This means to make use of the VTPC1 data (section 4.2.1).

4.1.3 Track Selection

For the signal quality the normalized signal charge, which is measured by QDC (Charge-Digital-Converter) for the track is restricted ($0.8 \leq q \leq 1.6$), and the tracks with hit position on each scintillator overlapped edge ($x \leq 1$ cm) are ignored.
Additionally, since each scintillator cannot resolve the simultaneous double hits from an event, only the tracks with a single hit per an event onto the same scintillator are selected.

4.1.4 Pair Selection

As two tracks within the same scintillator in a single event are not used in the construction of the original Q_{inv} distribution, the same condition has to be applied when calculating the mixed-events background.
The single hit constraint has a direct effect on the Q_{inv} distribution because two tracks with small momentum difference tend to hit the same TOF scintillator. This effect can be studied when constructing Q_{inv} distributions from the event-mix with and without the single hit constraint. Fig. 4.8(a) shows the condition that the two tracks must not be detected in the same scintillator reduces the efficiency below $Q_{inv} \approx 40$ MeV. Above $Q_{inv} \approx 20$ MeV the losses are smaller than 5%, so only this Q_{inv} region is considered to derive the invariant radius.

[6]Beam rapidity is 5.8, midrapidity is 2.9

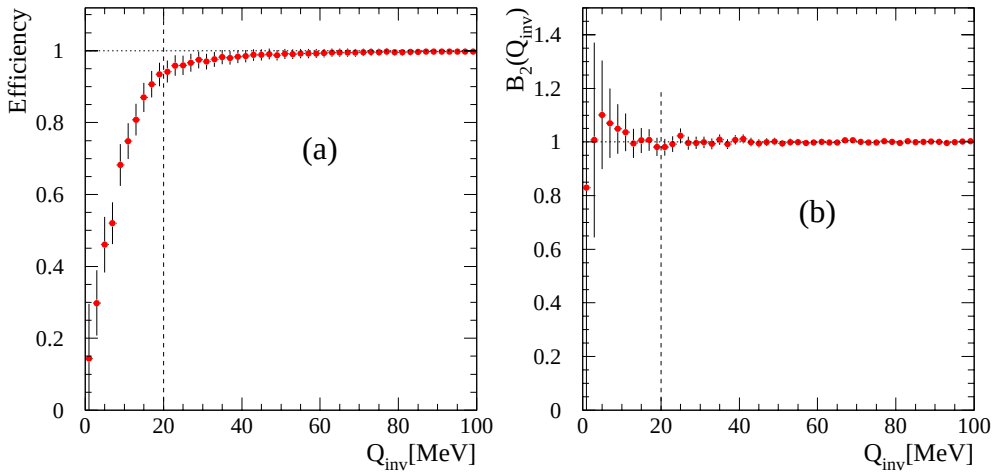

Fig. 4.8: (a) Single hit efficiency of TOF-R wall. The dashed line indicates the limit of the single particle constraint with 95% efficiency. (b) The ratio of the no constraint event mixing and the two particle constraint event mixing for positive kaons. The dashed line is the same as in (a).

4.1.5 Event Selection

By definition of two-particle correlation, only events with at least two kaons contribute to the original Q_{inv} distribution. Therefore, only such events can be used for the calculation of the mixed-events background.

This event selection can influence the HBT enhancement at a small value of Q_{inv}, because it is found that different-event mixing never fully removes the correlations induced by Bose statistics [Zaj84]. This is most easily appreciated by considering a hypothetical experiment that measures only a very small region of the total $\mathsf{p}_1 \approx \mathsf{p}_2$ phase space. As the size of this region decreases to zero, every real particle pair will be within the "range" of the correlation, so that $\mathsf{p}_1 \approx \mathsf{p}_2$ for all events, and thus any mixing process on this data set will also create events with $\mathsf{p}_1 \approx \mathsf{p}_2$.

The ratio $B_2(Q_{inv})$ of the no-constraint event mix and two-particle constraint event mix is calculated for positive kaons as shown in Fig. 4.8(b). One observes a non-physical fluctuation at small Q_{inv}. This region, however, will not be used for HBT radius extraction as explained in the previous section.

4.2 Pion Selection from VTPC1 Data

4.2.1 Acceptance Range of VTPC1

As shown in Fig. 4.9, the acceptance region of VTPC1 covers a large rapidity range, surely including the region of interest ($3 \leq \mathrm{Y} \leq 3.5$), which is indicated by the solid lines in Fig. 4.9. Only pions within this rapidity window are used for the HBT analysis.

4.2.2 Particle Identification by $\mathrm{d}E/\mathrm{d}x$

In analogy to Fig. 3.2, particle identification in VTPC1 is only possible using the $\mathrm{d}E/\mathrm{d}x$-information in each momentum bin. The corresponding diagram to the the-

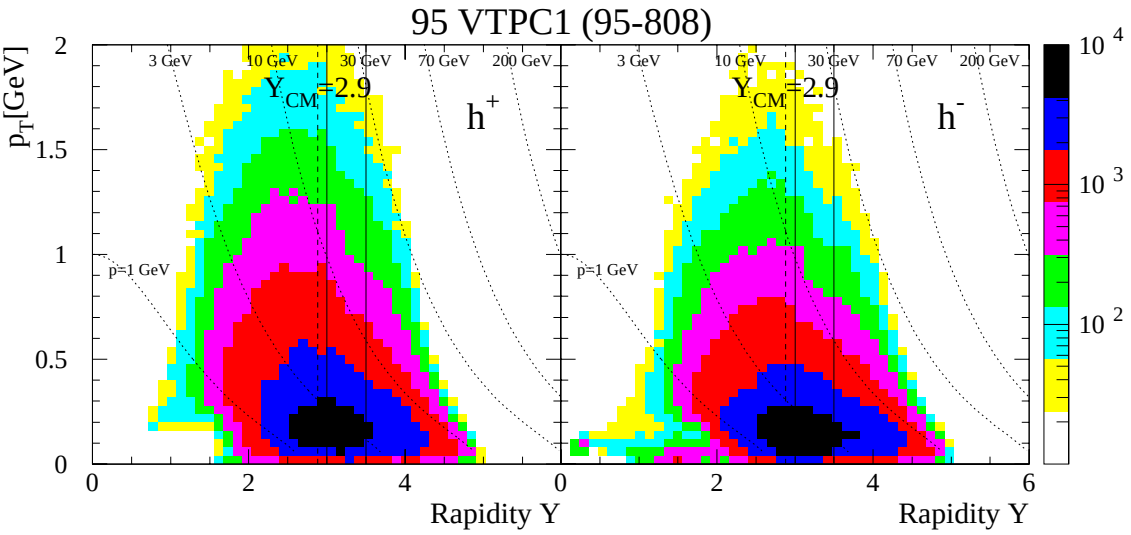

Fig. 4.9: Acceptance region of VTPC1 in rapidity Y and transversal momentum p_T. For demonstration purposes, only one RUN(95-808) is taken. The dashed line indicates the midrapidity Y_{CM}. In comparison with Fig. 4.7 only the rapidity range $3 \leq \mathrm{Y} \leq 3.5$, indicated by the solid lines, is chosen for the analysis.

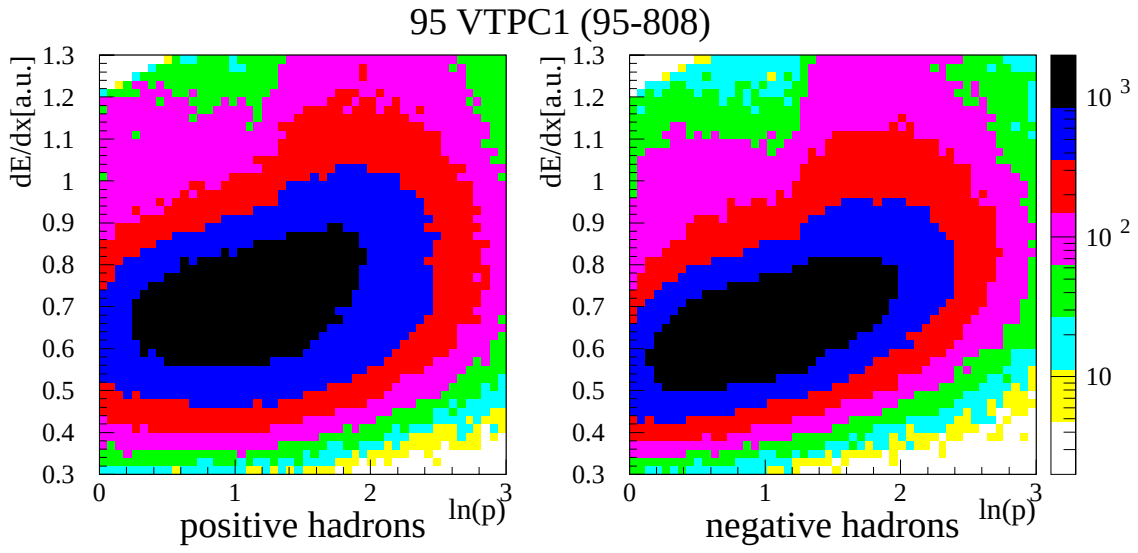

Fig. 4.10: Specific energy loss of particles detected by VTPC1 as a function of (logarithmic) momentum.

oretical calculation in Fig 3.2 is shown for VTPC1 data in Fig. 4.10. The separation capability is strongly limited compared to the use of combined TOF and $\mathrm{d}E/\mathrm{d}x$ measurement ; however, since the pion contribution is dominant, a rough selection can be done by a cut around the mean specific energy loss for pions and as a function of momentum.

As illustrated for instance in Fig. 4.11 (a) and (b), the specific energy loss distribution is composed of the Gaussian contributions of the different particle species. For positive particles, this distribution is decomposed to p+K^+, π^+ and e^+. In the case of negative particles, however, only the separation of electrons is possible, so that the $< \mathrm{d}E/\mathrm{d}x >$ values for negatively charged pions are systematically lower than positive ones (Fig. 4.11 (c) and (d)). Nevertheless, for the pion selection the region above $< \mathrm{d}E/\mathrm{d}x >$ is almost not contaminated by antiprotons and negative kaons.

In order to find out the proper fit to the distribution of the mean specific energy loss depending on the momentum, the well-known specific energy loss theory of Bethe [Bet32] and Bloch [Blo33] is used, which implies that the mean $\mathrm{d}E/\mathrm{d}x$ of all kinds of particles is a universal function of velocity. With the relation of $\beta\gamma = p/m$, and accordingly $\beta^2 = \frac{p^2/m^2}{1+p^2/m^2}$, the empirical Bethe-Bloch function [Fri99] can be applied

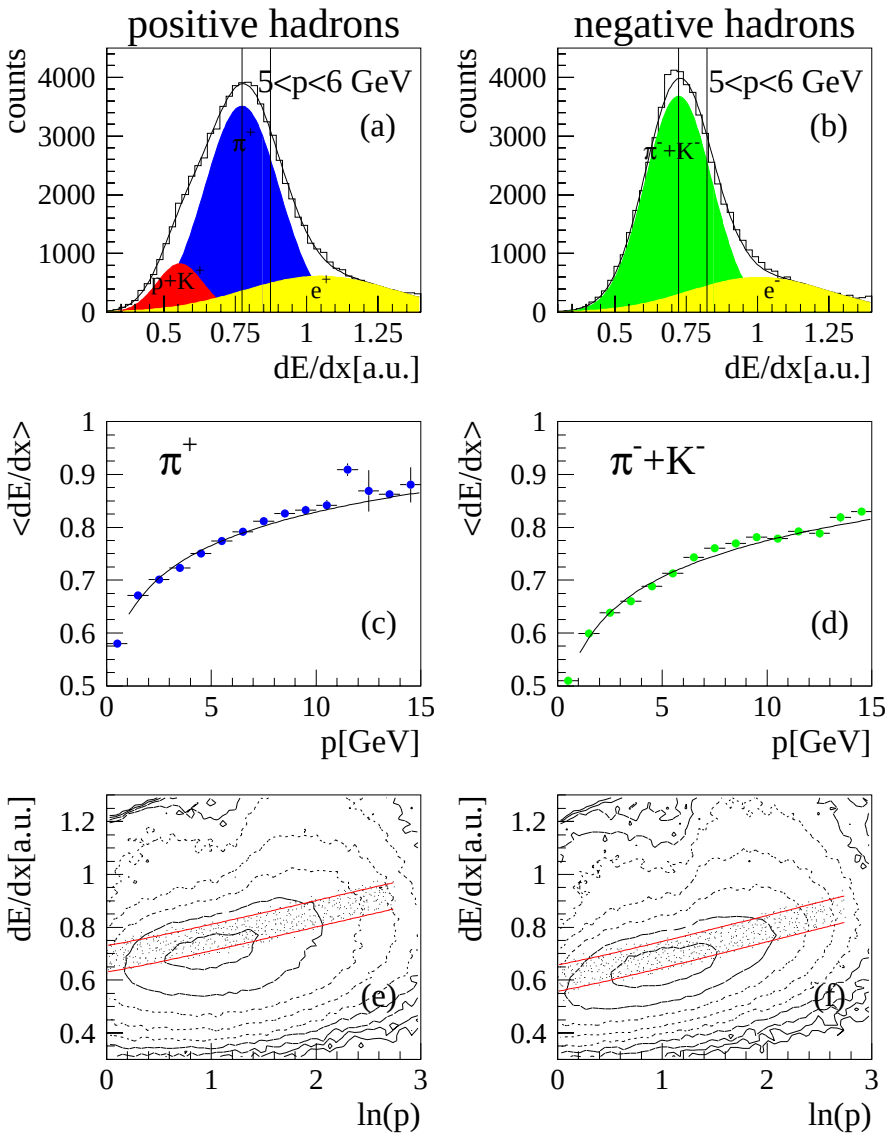

Fig. 4.11: (a) and (b) : The dE/dx distribution at a given momentum (here e.g. 5-6 GeV) and its decomposition into each particle contribution. The lines indicate the selection cut for pions. (c) and (d) : The mean dE/dx for pions as a function of momentum. The solid lines represent the fit result (see text). (e) and (f) : The pion cut (dark region) and the original dE/dx distribution, which is equivalent to Fig. 4.10.

to fit the momentum-dependent mean $\mathrm{d}E/\mathrm{d}x$ (Fig. 4.11 (c) and (d)) as follows :

$$< \frac{\mathrm{d}E}{\mathrm{d}x} > (\beta\gamma) = \frac{E_0}{\beta^2}(K + \ln\gamma^2 - \beta^2 - \delta(\beta, X_A, a)) \tag{4.4}$$

where $\gamma = (1-\beta^2)^{-\frac{1}{2}}$ and E_0, K are free parameters with X_A and a in the Fermi-density correction term δ, which is in accordance with [Ste71] and can be expressed as :

$$\delta(\beta, X_A, a) = \begin{cases} 0 & (X < X_0) \\ 4{,}605(X - X_A) + a(X_1 - X)^3 & (X_0 < X < X_1) \\ 4{,}605(X - X_A) & (X > X_1) \end{cases} \tag{4.5}$$

where $X = \log(\beta\gamma)$. Using this parameterization, the pion cut is defined as $< \mathrm{d}E/\mathrm{d}x >$ plus one standard deviation (solid lines in Fig. 4.11 (a) and (b)). Finally the particle identification of charged pions can be illustrated as the dark regions in Fig. 4.11 (e) and (f), which correspond to Fig. 4.10.
Unfortunately, the complete parameterization of $\mathrm{d}E/\mathrm{d}x$ including all particle species could not be done, because the $\mathrm{d}E/\mathrm{d}x$ resolution is not sufficient to decompose all particle sorts. In particular, the electron contamination[7] (approximately 10% for the complete momentum range) in the selected region has a certain influence upon the pion HBT analysis. This will be discussed in Section 6.

4.2.3 Track Selection

Since VTPC1 is located very close to the target, the track density is extremely high compared to the other tracking units. So, individual track points may be used several times by the track finding algorithm, leading to non-real tracks (so-called *ghost tracks*). They will on average have less points assigned to them as real tracks, but a straightforward cut in the number of track points cannot be easily found. Fig. 4.12 shows the distribution of the number of points assigned to a track for different combinations of tracking units, each including VTPC1. If the track point cut was chosen too large, one would loose many VTPC1-only (low-momentum) tracks, which would influence the HBT results. For determining an optimal cut in the number of track points, we study the two-track resolution of VTPC1.

[7] see Fig. 4.11 (a) and (b)

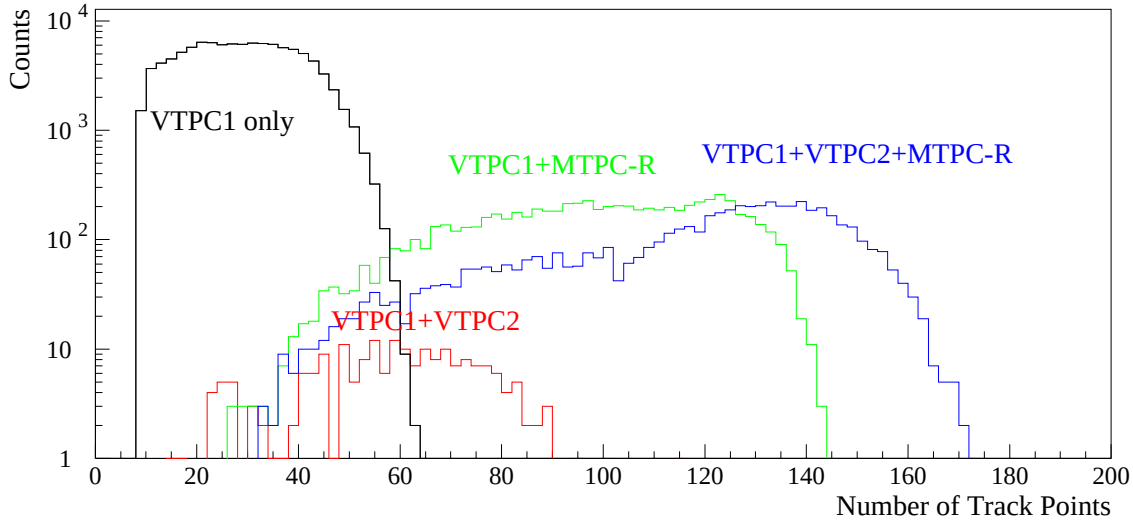

Fig. 4.12: Distribution of the number of track points of selected pion sample for various combinations of detector units.

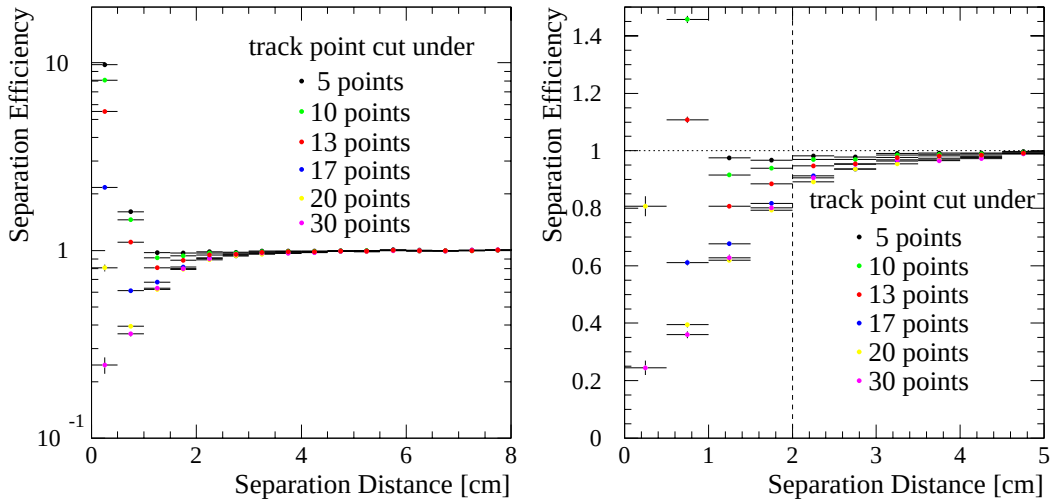

Fig. 4.13: The separation efficiency with various track point cuts. On the left side an overlook is shown in a logarithmic scale and on the right side it is magnified in linear scale.

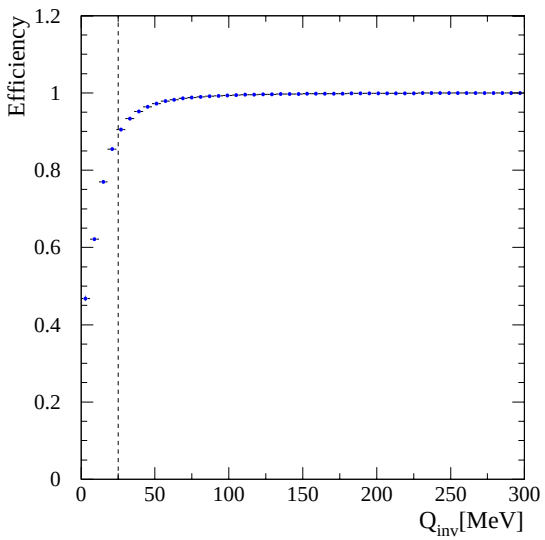

Fig. 4.14: The efficiency of Q_{inv} caused by cutting off of the very close tracks, whose distances are below 2 cm. The dashed line indicates the Q_{inv}-limit with 90% efficiency.

Let us consider two tracks (α and β) with spatial coordinates of the first (A) and the last (B) points in VTPC1 (x_{ij}, y_{ij}, z_{ij})[8], where i indicates point A or B, and j track α or β. Three reference planes are defined by $z_{init} := max(z_{A\alpha}, z_{A\beta})$, $z_{final} := min(z_{B\alpha}, z_{B\beta})$ and $z_{mid} := (z_{init} + z_{final})/2$. Assuming a straight track, the intersection with the middle plane can be calculated. As VTPC1 is located inside the magnetic field, the tracks are in reality curved, so this is an approximation only. The separation of two tracks is then defined as the mean of the intersection distances at the three reference planes.

Due to the finite two-track resolution of VTPC1, two spatially very close tracks in the same events will not be resolved, while this constraint does not hold for two tracks in different events, that is for event mixing. Thus, we define the separation efficiency as the ratio of the counts from the original events and from the mixed-events as shown in Fig. 4.13 for various track point cuts. Theoretically, the efficiency cannot be larger than unity and should decrease below the resolution of VTPC1. Contradictorily, the efficiency at small distances increases above unity (Fig. 4.13).

[8]The NA49 standard coordinate system is defined with respect to the center of the Vertex magnet 2 position (0,0,0) and beam direction (z-direction).

This increase is understood to be caused by ghost tracks.
With the track point cut of 13 points the decreasing pattern is remarkably observable below the distance of 2 cm, while the resolution limit of 2 cm begins to be destructed with more than 17 point cuts. Consequently, the data with the separation efficiency of more than 95% are available for HBT analysis of pions, with the track point cut of 13 points and the separation distance cut of 2 cm.
The effect of the 2 cm distance cut on the Q_{inv} distribution is shown in Fig. 4.14. In analogy to sections 4.1.4 and 4.1.5 this effect can be investigated by constructing the ratio of the event mix with 2 cm cut and without the cut. Below Q_{inv}=25 MeV the efficiency drops below 90%, thus only the Q_{inv}-region above 25 MeV will be used for the extraction of HBT radius parameters.

4.2.4 Event Selection

As the multiplicity of selected pions is about 26, the event constraint described for the event mix of the TOF kaons is not important for the pion sample.

Chapter 5

HBT Analysis

5.1 Construction of the Correlation Functions

In chapter 2, a theoretical expression for a two-particle correlation function was defined in terms of probability distributions of two-particle spectra. Experimentally, one does not measure probabilities directly, but rather yields or cross-sections. Since these quantities are proportional to the probabilities, one is able to substitute them into equation 2.12 obtaining :

$$C_2^{exp}(\mathsf{q},\mathsf{K}) = \mathcal{N}\frac{Y(\mathsf{p}_1,\mathsf{p}_2)}{Y(\mathsf{p}_1)Y(\mathsf{p}_2)} \tag{5.1}$$

where $Y(\mathsf{p}_1,\mathsf{p}_2)$ denotes the yield of a pair of the particle species from the same event with the momenta p_1 and p_2, or with the relative momentum q and average momentum K. The uncorrelated background for the denominator in Eq. 5.1 is generated by the event-mixing method [Kop74] that uses the yields of two particles from different events, and the normalization $\mathcal{N}$ denotes a factor so that the correlation function is defined to be unity at large relative momentum difference. Because the correlation is defined in terms of the ratio of the number of particle pairs, it is also referred to as *intensity interferometry*.

5.1.1 Gamov Coulomb Correction

Since the correlation functions that will be presented involve charged particles, they have to be corrected for the correlation introduced by the Coulomb repulsion, in order to get insight into the Bose-Einstein effect.
Until recently, most correlation functions were corrected by weighing each pair with a factor derived from the inverse Gamov factor, which is the square of the relative Coulomb wave-function of a particle pair at zero separation in the configuration space. It has the form [Mes91] :

$$G(\eta) = \frac{2\pi\eta}{e^{2\pi\eta} - 1} \tag{5.2}$$

with the Sommerfeld parameter :

$$\eta = \frac{2zz'\mu\alpha}{Q_{inv}} \tag{5.3}$$

where zz' is the product of electric charges, which is 1 for like-sign particles and -1 for unlike-sign ones, α is the fine-structure constant (1/137), μ is the reduced mass of the two-particle system, which is $\mu = m_i/2$ for two identical particles of species i, and Q_{inv} is the invariant 4-momentum difference of pairs. While the assumptions of a non-relativistic and point-like source made in the formulation of this factor are possibly appropriate for the sources investigated in e^+e^- or pp collisions, they are certainly not valid for the sources created in the current relativistic heavy-ion experiments at CERN. In fact, it has been shown that the use of the Gamov correction results in an underestimation of the source size [App97].
Therfore, there have been suggested so many Coulomb correction methods in [Alb97], [Bay96], [Bow91], [Pra86a] and [Sin98] etc. in order to solve the fundamental dilemma of Coulomb correction, that a Model, which is aimed by HBT analysis, should be introduced to calculate the Coulomb effect, which would have influence upon the HBT analysis.
Experimentally, the Coulomb correction can be obtained by measuring the correlation between unlike-sign particle pairs, which have only Coulomb correlations, but no Bose-Einstein effect. However, they might be influenced by different hadronic interactions (e.g. $K^+K^- \leftrightarrow \phi$). Since the inverse Coulomb correlation gained from unlike-sign pairs cannot be directly applied to correct the Coulomb attraction between like-sign pairs i.e. $G^{++}(\eta) = G^{--}(\eta) \neq 1/G^{+-}(-\eta)$, only some parameters,

which are used in the numerical function (section 5.1.2) and in the modified Gamov correction (section 5.1.3), can be extracted from the unlike-sign pair distribution.

5.1.2 Numerical Coulomb Correction

The standard Gamov factor is nothing but the squared amplitude of the Coulomb wave function $\psi_C(0)$, which is the solution of the Schrödinger equation of relative motion when both particles are in vanishing distance.

$$G(\eta) = |\psi_C(0)|^2 \tag{5.4}$$

In general, the solution with non-vanishing relative distance r is obtained by introducing the *confluent hypergeometric function*[1] given as :

$$\begin{aligned} \psi_C(\vec{r}) &= Ae^{iQz}F(-i\eta \mid 1 \mid iQ\cdot(r-z)), \qquad (5.7)\\ \text{where } A = \Gamma(1+i\eta)e^{-\frac{\pi\eta}{2}} &: \text{normalization factor,}\\ \eta = \frac{2zz'\mu\alpha}{Q} &: \text{Sommerfeld parameter,}\\ Q &: \text{relative momentum,} \end{aligned}$$

which can be numerically calculated [Nar92]. With simple hypothesis of isotropic Gaussian source distribution $S(r) = exp(-r^2/2r_0^2)$ with a standard deviation of r_0 and the function given in Eq. 5.7, the theoretical the Coulomb correction term can be numerically calculated as [Bay96] :

$$\frac{C_2^{exp}}{C_2^0} = \int \mathrm{d}^3r|\psi_C(\vec{r})|^2 S(r), \tag{5.8}$$

where C_2^0 denotes the correlation function in absence of Coulomb field.
In Fig. 5.3 for unlike-sign kaon pairs and Fig. 5.6 for unlike-sign pion pairs, this calculation and the experimental data are compared with the Gamov correction, and the appropriate parameter r_0 is to be extracted.

[1] A differential equation of the form

$$xy'' + (b-x)y' - ay = 0 \tag{5.5}$$

has a regular solution named *confluent hypergeometric function* defined as [Mes91] :

$$F(a \mid b \mid x) \equiv \sum_{n=0}^{\infty} \frac{(a)_n x^n}{(b)_n n!} = 1 + \frac{ax}{b1!} + \frac{a(a+1)x^2}{b(b+1)2!} + \cdots,\ b \neq 0, -1, -2, \ldots \tag{5.6}$$

5.1.3 Modified Gamov Correction

On the other hand, in order to account for the discrepancy of the Gamov correction the modified Gamov correction is suggested in [Bri95] as :

$$F(\eta) = (G(\eta) - 1) \cdot exp(-Q_{inv}/Q_{inv,eff}) + 1. \tag{5.9}$$

Phenomenologically, this modification is in the spirit of the Yukawa potential which is essentially an exponentially damped Coulomb potential [Las97]. Likewise, the phenomenological Coulomb correction is taken as an exponentially damped Gamov correction. For $Q_{inv,eff} \to \infty$ this term approaches the Gamov correction $G(\eta)$ - a point source, while in the opposite limit as it goes to 0, the function converges to unity - an infinite source.
This modified Gamov correction does not need any hypothesis of source distribution, and in general for anisotropic source distribution the relative momentum Q_{inv} and free parameter Q_{eff} can be decomposed, e.g. $q_\perp, q_\parallel, q_0$ in YKP-parameterization and free parameters $q_{i,eff}$ for each component as :

$$\frac{C_2^{exp}}{C_2^0} = (G(\eta) - 1) \cdot exp\left(-\sqrt{\sum_{i=\perp,\parallel,0} (\frac{q_i}{q_{i,eff}})^2}\right) + 1 \tag{5.10}$$

with $\eta = \frac{2zz'\mu\alpha}{\sqrt{q_\perp^2+q_\parallel^2+q_0^2}}$.
The exponential damping factors $q_{i,eff}$ are free parameters which are obtained by a 3-dimensional fit to the data. Fig. 5.10 for kaons and Fig. 5.13 for pions show the results for the correlation between unlike-sign particle pairs with comparison to the Gamov correction.

5.1.4 Estimation of Error Ranges

The errors of the parameters to be extracted are caused mainly by the following :

- statistical error : each yield in the distribution has the statistical error of the square-root of yield. Since the correlation function is the ratio of yield Y_S from the same event to yield Y_B from the mixed-events, the error ranges in the correlation distribution are to be bin-wise calculated by :

$$\sigma_{C_2} = \mathcal{N} \cdot \frac{Y_S}{Y_B}\sqrt{\frac{1}{Y_S} + \frac{1}{Y_B}} \tag{5.11}$$

where $\mathcal{N}$ is the normalization factor.

- Coulomb correction uncertainty : the uncertainty of the fit to the Coulomb correlation between unlike-sign particle pairs should influence the final parameters to be extracted from the corrected correlation function, and it is not analytically calculable. Examining these influences in case by case within the fit-error range, the mean of the maximum and minimum values of each parameter is taken with the error range of maximal deviation.

- Fit error : A 1-dimensional (or 3-dimensional) fit to the corrected C_2-distributions with a given error range is performed by the χ^2 minimizing method (or a maximum log-likelihood method), which delivers one standard deviation during the fit iterations as the fit-error. The fit results are given with the number of degree of freedom (N_{DF}) and χ^2/N_{DF}.

5.2 1-Dimensional Correlation Function

5.2.1 HBT Radius of Kaons

Raw Correlation Function

With 577k K^+K^+ pairs and 163k K^-K^- pairs from the dataset of 95 TOF-R, and with 458k K^+K^+ pairs and 214k K^-K^- pairs from 96 TOF-R/L, the C_2^{raw}-distributions for like-sign pairs are obtained separately, dividing the Q_{inv}-distribution from the same events by that from mixed-events[2]. Accordingly, their means weighted by signal entries are shown in Fig. 5.1, since the datasets of 95 and 96 have so different acceptance conditions respectively, that one cannot directly add the two datasets.
In both cases the enhancement caused by the Bose-Einstein correlation is obviously observable at Q_{inv} smaller than about 100 MeV in C_2^{raw} for K^+K^+ as well as for K^-K^-. A fluctuation or rapid decrease at $Q_{inv} \lesssim 20$ MeV should not be regarded because of the constraint effect as explained in the previous chapter. Nevertheless, the Coulomb effect is visible at $Q_{inv} \leq 40 MeV$ in the decrease of the raw correlation

[2]as explained on page 59

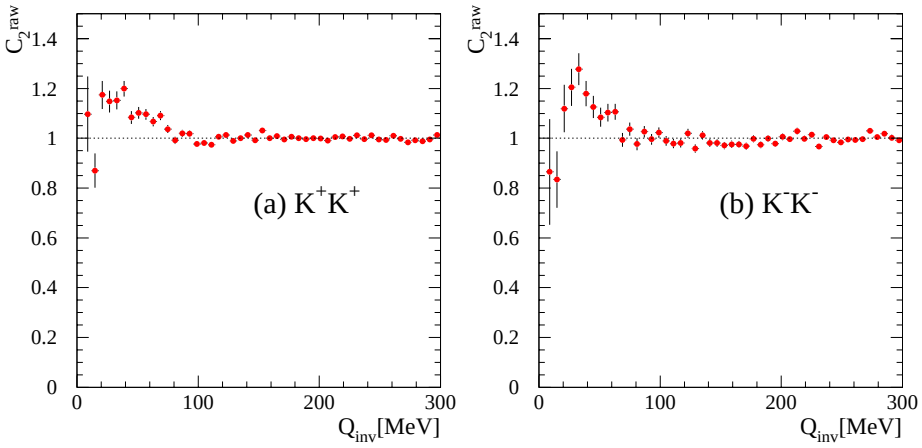

Fig. 5.1: The raw correlation function (a) between K^+K^+ pairs and (b) between K^-K^- pairs.

function.

Correlation between unlike-sign Kaons

For the sake of the Coulomb correction the correlation between unlike-sign kaons is investigated. Analogously, to the like-sign kaon analysis, the Q_{inv} distribution of K^+ and K^- pairs is respectively analyzed with 347.7 k pairs (STD-) and 249.3 k pairs (STD+) from the dataset of 95 TOF-R/L, and with 614.7 k pairs (STD+) from 96 TOF-R/L and in succession their weighted means are obtained in Fig. 5.3. In this case, as K^+ and K^- are detected in opposite TOF hemispheres, the detector constraint is not required.

However, a new aspect in the Q_{inv} distribution of K^+K^- is the ϕ-resonance, whose dominant decay channel is K^+K^-. The resonance region must be excluded for the normalization of the correlation function. Thanks to the support of Dr. V. Friese, who has studied ϕ production in the same dataset [Fri99], the Q_{inv} distribution from ϕ-decay is simulated within the TOF acceptance. The ϕ simulation parameters are shown in Tab. 5.1. From the randomly generated ϕ mesons, about 49 % of them decay to K^+ and K^-, which are detected in the TOF-R and TOF-L walls, respec-

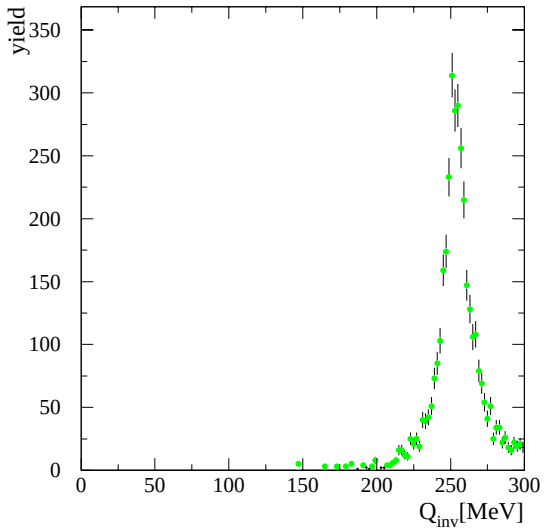

Fig. 5.2: The simulated Q_{inv} distribution of K^+ and K^- from the ϕ resonance.

tively. The distribution of their 4-momentum differences Q_{inv} is shown in Fig. 5.2. It is no surprise, that the resonance shows up around $Q_{inv} \approx 250$ MeV, since this is the momentum difference of the decay products in the rest frame of the ϕ-meson [PDG98]. This ϕ-resonance peak is experimentally also observable in Fig. 5.3. It must be excluded for the normalization of the correlation function. Accordingly, the normalization range from 300 MeV to 2000 MeV is taken.

The Coulomb correlation between unlike-sign kaons enables one to extract the parameter r_0 to about 27 fm indicated as the solid line in Fig. 5.3, while the Gamov correction (i.e. r_0= 0 fm) indicated as the dotted line in the figure does not describe

# of generated ϕs	10,000,000
mass mean of ϕ [GeV]	1.0191
mass width of ϕ [MeV]	4.4300
mass resolution [MeV]	1.2000
std. deviation of rapidity distribution of ϕ	1.2500
temperature of ϕ [MeV]	295.0000

Table 5.1: The parameters of simulation of ϕ-decay to K^+ and K^- [Fri99a]

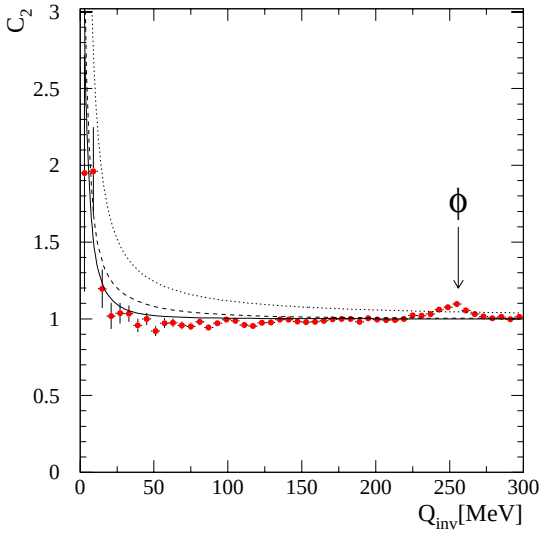

Fig. 5.3: Q_{inv} distribution of K^+ and K^- pairs from the data of TOF-R/L. The solid and dotted lines denote the calculated function and the Gamov correction, respectively. The dashed line calculated with $r_0 \approx 7$ fm does not describe the data (see text).

the data. However, such a Gaussian source distribution with the extracted standard deviation $r_0 = 27$ fm is physically impossible, considering the scale of the classical turning radius r_t, which is defined by :

$$\frac{Q^2}{2\mu} = \frac{e^2}{r_t}, \tag{5.12}$$

and $r_t \approx 7$ fm for the kaon. This discrepancy can be caused by anisotropic or non-Gaussian source distribution. The numerical calculation with $r_0 \approx 7$ fm is shown as the dashed line in Fig. 5.3.

On the other hand, using the modified Gamov correction function (Eq. 5.9) one obtains $Q_{inv,eff} = 15$ MeV, which describes the experimental data very well just like the solid line in Fig. 5.3. Because of its consistency this modified Gamov function with $Q_{inv,eff} = 15$ MeV is used for the Coulomb correction. In addition, since the physically reliable calculation (the dashed line in the figure $r_0 \approx 7$ fm) underestimates the final result of R_{inv} by about 10%, this correction uncertainty is also included in the error range of the final result (Fig. 5.4).

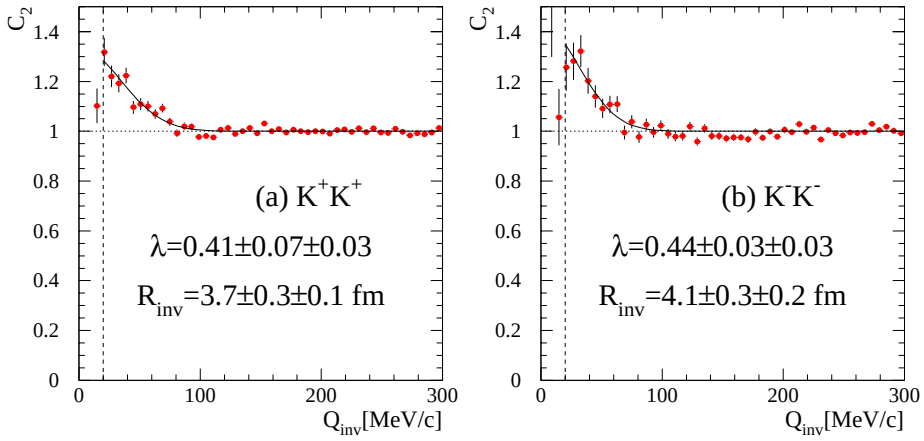

Fig. 5.4: The Coulomb corrected 1-dimensional correlation function between like-sign kaons. The solid lines indicate the proper fit to the data by Eq. 2.20 with parameters given in the results. The dashed line gives the Q_{inv}-limit due to the detector constraint.

The Coulomb-corrected Correlation Function between like-sign Kaons

Dividing the raw correlation functions between like-sign kaon pairs (Fig. 5.1) by the Coulomb correction function, explained in the previous subsection with an exchanging of the sign of η, the final 1-dimensional correlation function is obtained (Fig. 5.4).

A fit of this function in Eq. 2.20 to these final correlation functions leads to the chaoticity parameter λ and the Lorentz-invariant HBT radius R_{inv}. They are obtained as $\lambda = 0.41 \pm 0.07 \pm 0.03$, $R_{inv} = 3.7 \pm 0.3 \pm 0.1$ for K^+K^+ and $\lambda = 0.44 \pm 0.03 \pm 0.03$, $R_{inv} = 4.1 \pm 0.3 \pm 0.2$ for K^-K^-. The errors include the uncertainties in the Coulomb corrections. These parameters will be interpreted and compared with those of pion in Section 5.2.3.

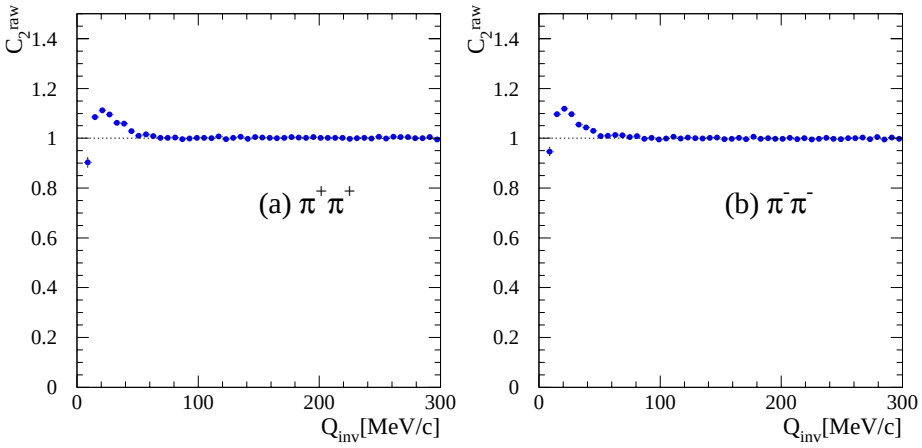

Fig. 5.5: The raw correlation function (a) between positively charged pions and (b) between negatively charged pions.

5.2.2 HBT Radius of Pions

Raw Correlation Function

Analogously to the case of the kaon analysis the Q_{inv} distribution between like-sign pions is calculated from 17.7M positive pion pairs and 18.5M negative pion pairs selected from VTPC1 data as explained in section 4.2.
In Fig. 5.5 one observes the clear Bose-Einstein enhancement at low Q_{inv} and the rapid decreasing at $Q_{inv} \approx 0$ due to the Coulomb repulsion, which should be corrected by the correlation between unlike-sign pions.

Correlation between unlike-sign Pions

The Q_{inv} distribution of unlike-sign pion pairs is obtained from 17.0M pion pairs form VTPC1 data as shown in Fig. 5.6.
In accordance to Eq. 5.8 the parameter r_0 is determined as 6 fm for an appropriate description of the data distribution and indicated as the solid line in Fig. 5.6. As denoted by the dashed line, the standard Gamov correction does not describe the data.

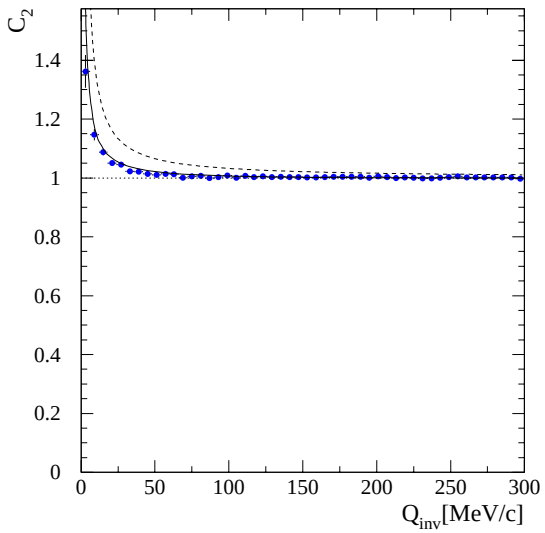

Fig. 5.6: The Coulomb correlation between unlike-sign pions. The solid line indicates the numerically calculated Coulomb correlation function with the parameter $r_0 = 6$ fm in Eq. 5.8 and for comparison the standard Gamov correction function is shown by the dashed line.

Correlation Function between like-sign Pions

Finally, the Coulomb corrected correlation between like-sign pions is obtained as shown in Fig. 5.7 after bin-wise dividing the raw correlation in Fig. 5.5 by the numerically calculated correction function with an exchanging the sign of η in Eq. 5.8.

The proper fit to data with the parameters of Eq.2.20 is performed excluding the first three bins due to the constraint of pair selection as discussed in Section 4.2.3. The obtained parameters are $\lambda = 0.26 \pm 0.01$, $R_{inv} = 5.4 \pm 0.1$ for $\pi^+\pi^+$ and $\lambda = 0.27 \pm 0.01$, $R_{inv} = 5.7 \pm 0.1$ for $\pi^+\pi^+$.

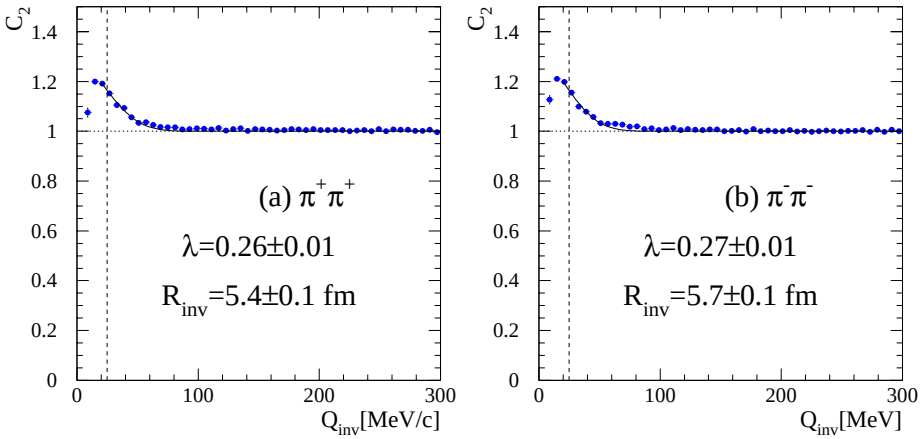

Fig. 5.7: The Coulomb corrected 1-dimensional correlation function between like-sign pions. The solid lines indicate the proper fit to the data by Eq. 2.20 and the extracted parameters are in each figure.

5.2.3 Comparison of R_{inv} for Kaons and Pions

Comparing the invariant radius R_{inv} of kaons with that of pions, one has to realize that they contain spatial as well as temporal information. This can be seen when factorizing the expansion of Eq. 2.20 into :

$$C_2 = 1 + \lambda e^{-|\vec{q}|^2 R^2 - q_0^2 \tau^2}. \tag{5.13}$$

From the general relation $q_0 = \vec{q} \cdot \vec{\beta}_{pair} = |\vec{q}||\vec{\beta}_{pair}|\cos\theta$ (where $\vec{\beta}_{pair}$ is the velocity of the pair frame relative to the reference frame), the spatial and invariant radii of Eqs. 2.20 and 5.13 can be related [Aki93] via

$$\left(\frac{R_{inv}}{R}\right)^2 = \frac{1 + (\tau^2/R^2)|\beta_{pair}|^2\cos^2\theta}{1 - |\beta_{pair}|^2\cos^2\theta}. \tag{5.14}$$

For this equation it is clear that R_{inv} represents an average over an ensemble of pair rest frame, so that the relation between R_{inv} and R may be different for kaons and pions.

The distributions of $|\beta_{pair}|$ and $\cos\theta$ in the nucleon-nucleon center-of-mass frame for pairs used for the analysis are shown in Fig. 5.8. Clearly, the distributions of pion and kaon pairs are significantly different. This explicitly demonstrates that

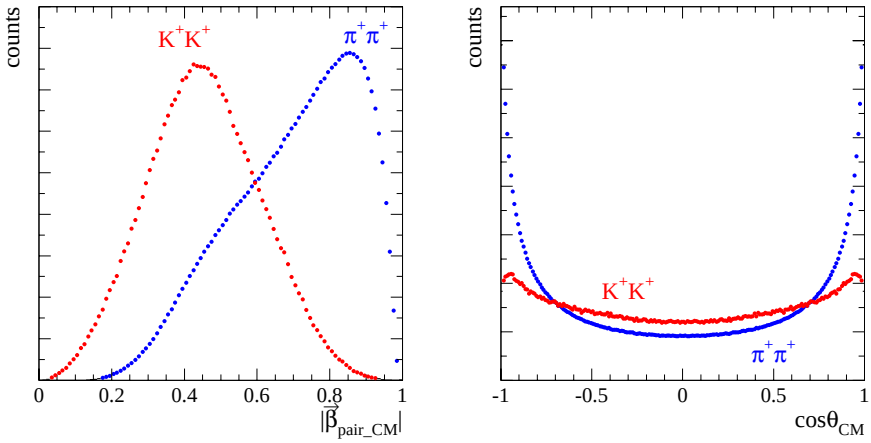

Fig. 5.8: The distribution of $|\beta_{pair}|$ and cosθ in the nucleon-nucleon center-of-mass frame for kaon pairs and pion pairs

R_{inv} measures a *Lorentz extended* value of the source radius R as viewed from the pair rest frame [Sin89]. Note that the size of this effect depends on the magnitude and direction of $\vec{\beta}_{pair}$, and that *these factors are significantly different for kaons and pions*.

Under the assumption of $R \approx \tau$ the relatively well known pion results [Abb92], the transformation factor R_{inv}/R is calculated pairwise. The mean values of R_{inv}/R and the transformed results are summarized in Tab. 5.2. In addition, the 3-dimensional effective radius R_{rms} is calculated as $R_{rms} = \sqrt{\sum_{i=1}^{3} < x_i^2 >} = \sqrt{3}R$.

Even though the Lorentz-invariant radii of kaons and pions are quite different as shown in Tab. 5.2, **the transformed spatial radii of kaons and pions in the reference frame are quite similar**.

Particle	λ	R_{inv} [fm]	$< R_{inv}/R >$	R [fm]	R_{rms} [fm]
K^+	0.41±0.10	3.7±0.4	1.12±0.05	3.3±0.5	5.7±0.8
K^-	0.44±0.06	4.1±0.5	1.11±0.05	3.7±0.6	6.4±0.9
π^+	0.26±0.01	5.4±0.1	1.53±0.12	3.5±0.3	6.1±0.5
π^-	0.27±0.01	5.7±0.1	1.51±0.12	3.8±0.4	6.5±0.7

Table 5.2: The extracted parameters and the transformed radii for kaons and pions

5.3 3-Dimensional Correlation Function

As given in Eq. 2.32, the correlation function was parameterized by Yano, Koonin and Podgoretskii in terms of $q_\perp$, q_0 and $q_\parallel$ as [3] :

$$C_2 = 1 + \lambda exp\left[-q_\perp^2 R_\perp^2 - \gamma_{YK}^2 (q_\parallel - v_{YK} q_0)^2 R_\parallel^2 - \gamma_{YK}^2 (q_0 - v_{YK} q_\parallel)^2 R_0^2\right] \quad (5.16)$$

In general, the longitudinal velocity v_{YK} depends on the pair mean momentum K. Accordingly, this analysis should be performed in each K-bin, in particular in each $|\vec{K}_T|$-bin for the investigation of the transversal freeze-out configuration, just like the rapidity range is here restricted for the longitudinal freeze-out configuration. Since the kaon statistics is, however, not sufficient to be analyzed in each $|\vec{K}_T|$-bin, in this thesis the 3-dimensional analysis is performed over the complete range of $|\vec{K}_T|$ or $|\vec{p}_T|$, which is distributed with a similar mean value of about 0.2 GeV/c for pions and kaons as shown in Fig. 4.7 and 4.9.

5.3.1 HBT Radii of Kaons

Raw Correlation

The correlation functions with the YKP-parameterization without Coulomb correction are shown in Fig. 5.9, as 1-dimensional projections with the other components being restricted to below 30 MeV. In these projections the counts at small q_i are suppressed, due to the detector constraints and the Coulomb repulsion. In particular the limited q_0 ranges in Fig. 5.9 (b) and (e) are due to the relation 2.36.

[3] where

$$\begin{aligned} q_\perp &= |\vec{q}_T| \\ q_0 &= E_1 - E_2 \\ q_\parallel &= q_z \end{aligned} \quad (5.15)$$

in Fig. 2.2.

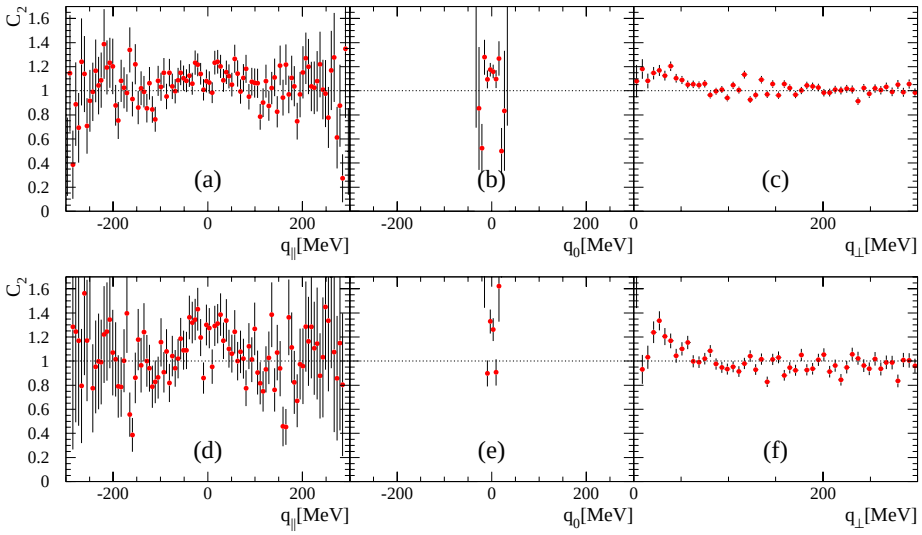

Fig. 5.9: 1-dimensional projections in q_i of the 3-dimensional distributions with $q_j \leq 30$ MeV ($j \neq i$) (a), (b) and (c) are for K^+K^+ correlation, and (d), (e) and (f) are for K^-K^- correlation.

Coulomb Correlation between unlike-sign Kaons

Analogously to the 1-dimensional analysis, the 3-dimensional correlation between unlike-sign particles gives information about Coulomb attraction, which do not need to be symmetric in 3-dimension. The 1-dimensional projections (perpendicular components < 12 MeV) are shown in Fig. 5.10.

A three-dimensional fit of the function 5.10 to the data distribution is performed and the results are given in Tab. 5.3. This effective Coulomb correction influences

$Q_{\parallel,eff}$	25 ± 3 MeV
$Q_{\perp,eff}$	20 ± 5 MeV
$Q_{0,eff}$	48 ± 10 MeV
N_{DF}	459
χ^2/N_{DF}	1.17

Table 5.3: The parameters of the Coulomb correction function (Eq. 5.10) obtained by the unlike-sign kaon pairs. (Fig. 5.10).

mostly the first two bins of the raw like-sign correlations, which will be excluded for the extraction of HBT radii. The other data points are slightly corrected or unchanged. However, this slight correction of the data points around $q_i \approx 40 MeV$ is most sensitive to the extraction of HBT radii. For comparison to the Gamov correction is indicated in Fig. 5.10 as the dashed lines, clearly the effective Coulomb correction in this range is much more appropriate than the Gamov correction. (The ϕ-meson seen in Fig. 5.3 is here outside of the range used for the projections.)

The Coulomb-corrected Correlation between like-sign Kaons

By dividing the raw correlations by the Coulomb corrections, the 3-dimensional correlation functions are obtained as shown in Fig. 5.11. According to Eq. 5.16 the fit results obtained by the negative log-likelihood method are drawn in each figure and the extracted HBT radii and parameters are listed in Tab. 5.4.

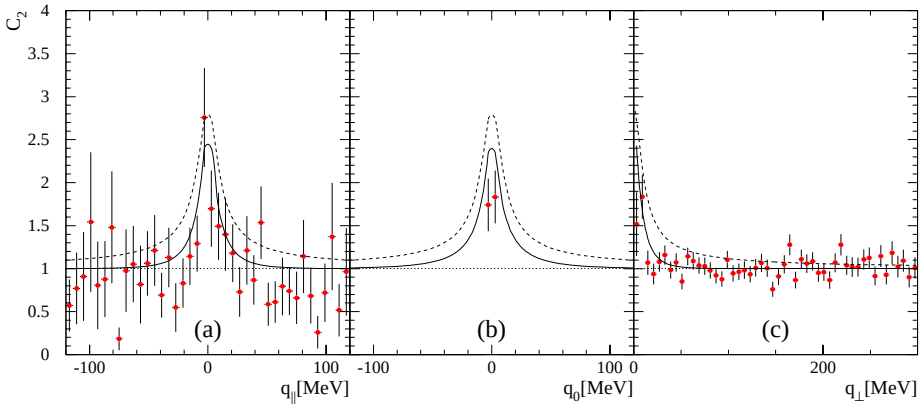

Fig. 5.10: 1-dimensional projections of the 3-dimensional distributions between unlike-sign kaons, the perpendicular components being restricted to < 12 MeV. The solid lines in each histogram indicate the proper fit to data by Eq. 5.10, whose extracted parameters are listed in Tab. 5.3. For the sake of comparison, the Gamov corrections are indicated by the dashed lines in each histogram.

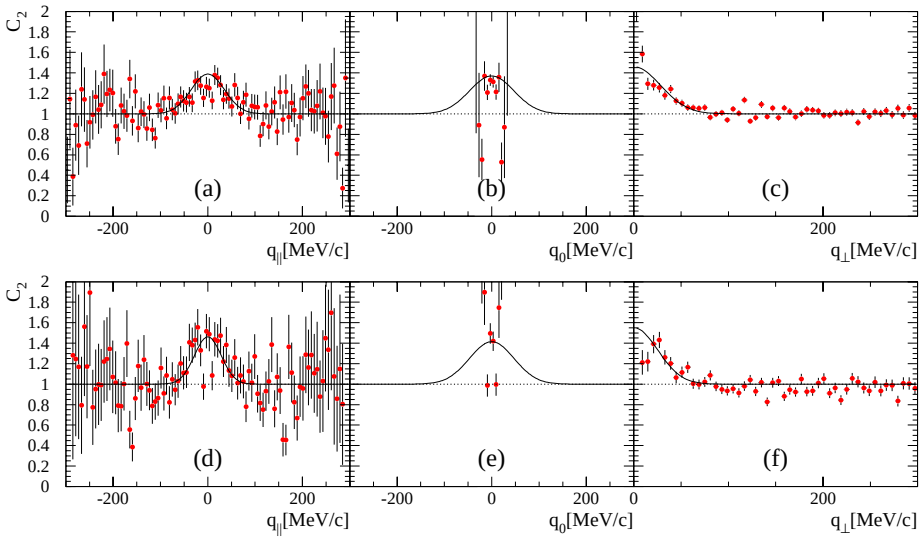

Fig. 5.11: 1-dimensional projections in q_i of the Coulomb-corrected 3-dimensional correlation between like-sign kaons with $q_j \leq 30$ MeV ($j \neq i$). The solid lines in each histogram indicate the proper fit to data by Eq. 5.16 with parameters given in Tab. 5.4

	λ	$R_{\|\|}[fm]$	$R_{\perp}[fm]$	$R_0[fm]$	v_{YK}	N_{DF}	χ^2/N_{DF}
K^+	0.55 ± 0.05	4.5 ± 1.0	4.9 ± 0.4	3.0 ± 1.2	0.04 ± 0.03	386	1.25
K^-	0.65 ± 0.08	4.9 ± 1.2	5.5 ± 0.8	3.0 ± 1.5	0.03 ± 0.02	891	1.15

Table 5.4: The extracted parameters of the 3-dimensional fit to the corrected correlation function for kaons (Fig. 5.11).

Varying the fit ranges and excluding the detector constraint q_i ranges, error estimates of the fit results are obtained. The final results will be discussed together with those of pions in the next chapter.

5.3.2 HBT Radii of Pions

Raw Correlation

Just like in the case of kaons, the 3-dimensional distributions for like-sign pion pairs are calculated and the results are as shown in Fig. 5.12. As one observes, the enhancement at $q_i \leq 50$ MeV and the slight breakdown at $q_i \approx 0$ reflects the Bose-Einstein correlation and the Coulomb repulsion or the inefficiency due to the detector constraint, respectively.

Coulomb Correlation between unlike-sign Pions

In order to obtain the Coulomb correction, the 3-dimensional correlation between unlike-sign pion pairs is calculated as shown in Fig. 5.13. The Coulomb attraction

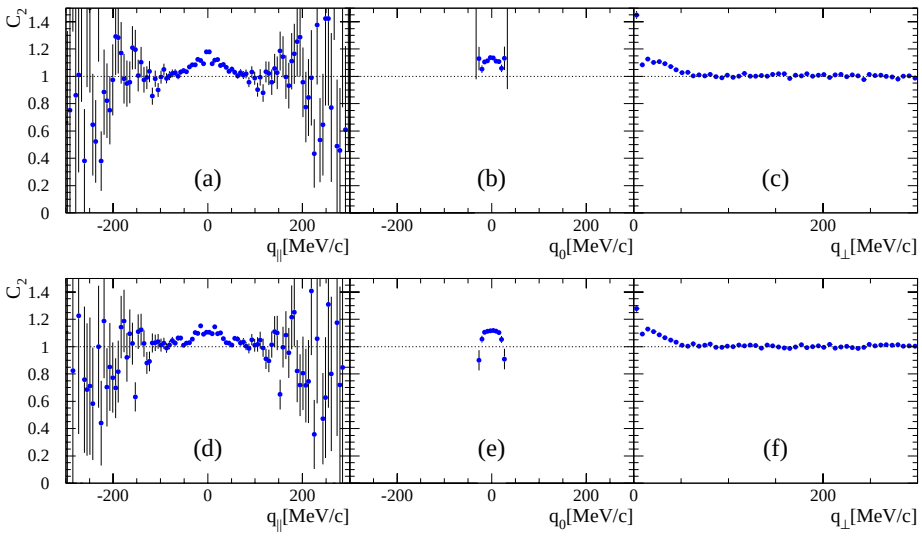

Fig. 5.12: 1-dimensional projections on each component of the 3-dimensional distributions, the perpendicular components being less than 30 MeV. (a), (b) and (c) are for $\pi^+\pi^+$ correlation, and (d), (e) and (f) are for $\pi^-\pi^-$ correlation.

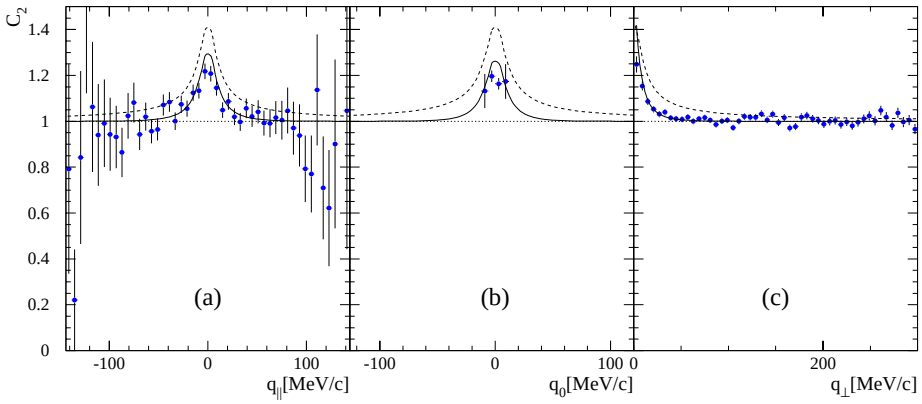

Fig. 5.13: 1-dimensional projections onto each component of the 3-dimensional correlation between unlike-sign pions, the perpendicular components being less than 12 MeV.

$Q_{\parallel,eff}$	27 ± 5 MeV
$Q_{\perp,eff}$	22 ± 3 MeV
$Q_{0,eff}$	20 ± 5 MeV
N_{DF}	2609
χ^2/N_{DF}	1.08

Table 5.5: The parameters of the Coulomb correction function (Eq. 5.10) obtained by the unlike-sign pion pairs. (Fig. 5.13).

between unlike-sign pions obviously appears at $q_i \leq 40$ MeV and is fitted with the function given in Eq. 5.10. In Tab. 5.5 the extracted parameters are listed. Dividing the raw correlation between like-sign pions (Fig. 5.12) by this fit function and exchanging the sign of η in Eq. 5.10, the effective Coulomb correction is performed.

The Coulomb-corrected Correlation between like-sign Pions

The corrected correlation function is presented in 1-dimensional projections, as shown in Fig. 5.14. In order to extract the radii and other parameters, the 3-dimensional distribution is fitted by Eq. 5.16 using the negative log-likelihood method

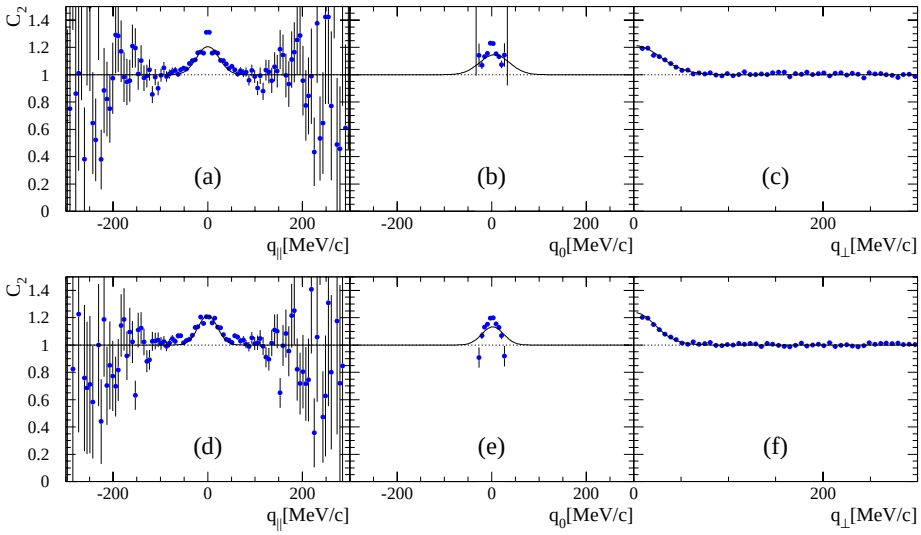

Fig. 5.14: 1-dimensional projections onto each component of the 3-dimensional correlation between unlike-sign pions, the perpendicular components being less than 30 MeV.

	λ	$R_{\|\|}[fm]$	$R_{\perp}[fm]$	$R_0[fm]$	v_{YK}	N_{DF}	χ^2/N_{DF}
π^+	0.28 $\pm$ 0.07	6.0 $\pm$ 0.5	5.0 $\pm$ 0.5	4.0 $\pm$ 0.8	0.10 $\pm$ 0.05	1362	1.02
π^-	0.34 $\pm$ 0.08	6.9 $\pm$ 0.8	6.0 $\pm$ 0.7	5.1 $\pm$ 1.5	0.06 $\pm$ 0.05	1128	1.12

Table 5.6: The extracted parameters of the 3-dimensional fit to the corrected correlation function for pions (Fig. 5.14).

by excluding the first two bins near $q_i \approx 0$.

In Tab. 5.6 the extracted parameters are listed. The error range is calculated with the Coulomb correction errors and the fit errors.

Chapter 6

Discussion

The results of the analysis described in the previous section are compiled in Tab. 6.1 with R_{rms} from Tab. 5.2. We discuss here a few aspects important for their interpretation.

6.1 Central Coulomb Effect

The first one of them is *the central Coulomb effect* [Bay96] in the system of Pb+Pb central collisions at 158 AGeV. In the collisions of nuclei, there exists a central Coulomb potential produced by the positive charge of the protons. Even though the Coulomb effect between the two particles of a pair is investigated and corrected in

	λ	$R_{\parallel}[fm]$	$R_{\perp}[fm]$	$R_0[fm]$	v_{YK}	$R_{rms}[fm]$
K^+	0.55 ± 0.05	4.5 ± 1.0	4.9 ± 0.4	3.0 ± 1.2	0.04 ± 0.03	5.7 ± 0.8
K^-	0.65 ± 0.08	4.9 ± 1.2	5.5 ± 0.8	3.0 ± 1.5	0.03 ± 0.02	6.4 ± 0.9
π^+	0.28 ± 0.07	6.0 ± 0.5	5.0 ± 0.5	4.0 ± 0.8	0.10 ± 0.05	6.1 ± 0.5
π^-	0.34 ± 0.08	6.9 ± 0.8	6.0 ± 0.7	5.1 ± 1.5	0.06 ± 0.05	6.5 ± 0.7

Table 6.1: The summary of the extracted parameters of 3-dimensional HBT analysis of kaon and pion, compared to the one-dimensionally obtained R_{rms}.

order to remove the final state interaction from the freeze-out state of the particles, there remains the question of the influence of the Coulomb interactions with the other particles.

In general, this is a difficult many-body problem. It can be greatly simplified with an assumption that the remaining particles can be described by a central Coulomb potential, $Z_{eff}e^2/r$, where the effective charge Z_{eff} is order of the total initial nuclear charge $(Z_A + Z_B)$ in a central collision of nucleus A with nucleus B. This central potential accelerates positive mesons away and slows down the negatives; these effects are described by the Coulomb wave functions for the potential. The final momentum of any particle is related to the initial momentum p_a at the production distance r_a by

$$\epsilon(p) = \epsilon(p_a) \pm \frac{Z_{eff}e^2}{r_a}, \tag{6.1}$$

where $\epsilon(p) = (p^2 + m^2)^{1/2}$. (While Coulomb effects for the relative momentum can be treated non-relativistically, the individual momenta are generally relativistic.) Since the Coulomb interaction conserves the total momentum of the pair $(n(\vec{p})\mathrm{d}^3p = n(\vec{p_a})\mathrm{d}^3p_a)$, the single particle distribution is modified by the central potential by

$$n(\vec{p}) = n_0(\vec{p_a})\frac{\mathrm{d}^3p_a}{\mathrm{d}^3p} = \frac{p_a\epsilon(p_a)}{p\epsilon(p)}n_0(\vec{p_a}), \tag{6.2}$$

where the subscript 0 indicates the 'initial' state.

Although the central potential shifts the single particle distribution, it cannot introduce any correlations among emitted particles that have no initial correlation in the absence of the central potential. If in the absence of the central potential uncorrelated particles $[C(q) = 1]$ are emitted in independent free particle states, then in the presence of the potential they are emitted in Coulomb states for the central potential, but still $n_2(\vec{p}_2, \vec{p}_2) = n(\vec{p}_1)n(\vec{p}_2)$ and $C(q)$ remains unity.

Since positive particles are accelerated, the final momentum difference, $\vec{q} = \vec{p}_1 - \vec{p}_2$, of a positive pair will generally be larger in magnitude than it initially is, while for negative pairs the final momentum difference will generally be smaller. Thus it is expected, that **the central Coulomb potential causes the size of the collision volume extracted from positive pairs to be smaller than the actual size, and that from negative pairs to be larger than the actual size [Bay96] [Har98]**. The final momentum difference q is therefore related to the initial

momentum difference q_a by

$$q \simeq q_a \left(1 \pm \frac{Z_{eff} e^2 / r_a}{p_a}\right) \tag{6.3}$$

where the upper sign refers to both particles being positively charged and the lower sign to both being negatively charged.
Here, the tendency appears between the extracted radii of positive particles and negative particles, even though the difference is within the error ranges. In our experiment the effect is an increase for positives (and a decrease for negatives) in the observed scale of $C(q)$ and a decrease (an increase) in the extracted radius of more than 10% and it is theoretically explained with Z_{eff} =164, the expected $r_a \approx 5$ fm for kaons and 6 fm for pions and supposingly $p_a \approx 300$ MeV/c in Eq. 6.3. This can also be seen in from Tab. 5.2 for the 1-dimensional analysis.

6.2 Comparison of the Results for Kaons and Pions

The second subject to be discussed is the comparison between the results for kaons and pions, and a physical understanding of the difference.
The R_{rms}, which are calculated from 1-dimensional analysis, are roughly comparable with $R_\perp$ and $R_\parallel$ within the error range, even though in the case of kaons the R_{rms} is somewhat larger than 3-dimensional spatial radii. This means, that the transformation from R_{inv} to R_{rms} works quite well in spite of a rough assumption $R \approx \tau (\equiv R_0)$ in Eq. 5.14.

The small values of v_{YK} show that the particles possess almost central rapidity when comparing Y_{CM} to the YKP-rapidity Y_{YKP} derived from v_{YK} by

$$Y_{YKP} = \frac{1}{2} \ln \frac{1 + v_{YK}}{1 - v_{YK}} + Y_{CM} \tag{6.4}$$

where $Y_{CM} = 2.9$.

The difference of the chaoticity parameters λ of pions and kaons can be explained

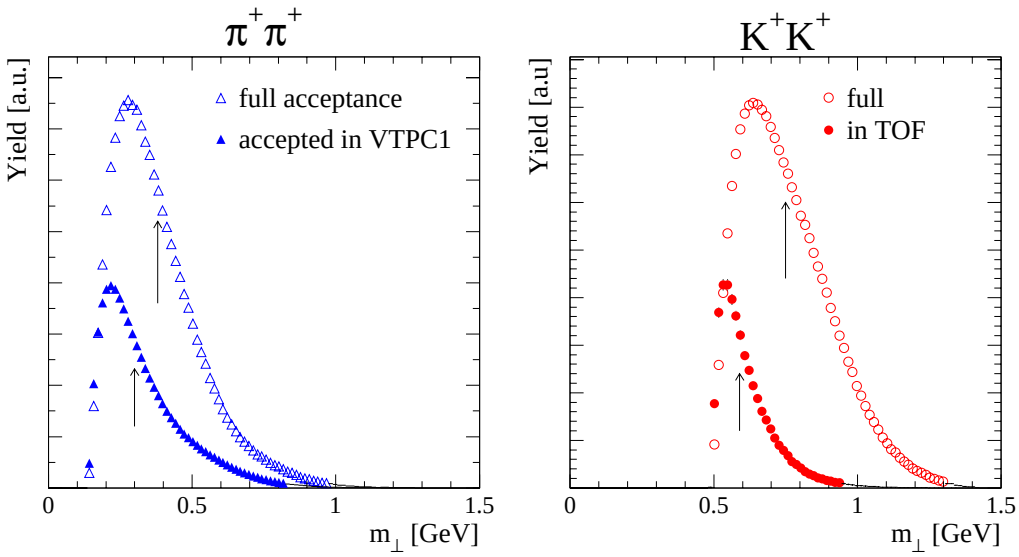

Fig. 6.1: Comparison of the $m_\perp$-distributions in the detector acceptance to those in the full acceptance. The arrows indicate the mean values of each distributions.

by the different influence of resonance decays, particularly long lived ω, η and η', which contribute to the pion multiplicity. In addition, the contamination of pions by electrons is relative large[1], which can cause the decrease of λ, while in the case of the kaon the anti-correlated protons are almost perfectly excluded by TOF particle identification.

The following discussion is based on two assumptions :
a) The freeze-out surface is identical for K and π. (This is supported by the data shown in the previous sections.)
b) The transverse expansion is small compared to that in longitudinal direction.
Remembering the relation Eq. 2.40 in case of the expanding source, the HBT radii are plotted as the function of the transversal mass $m_\perp = \sqrt{m_i^2 + K_\perp^2}$ (Fig. 6.2), where i denotes the particle species and the dashed line in the figure indicates $\sim m_\perp^\alpha$ as a reference. According to the theory suggested by U. Heinz [Hei96], the HBT radii parameters obey the $m_\perp$-scaling in the absence of collective transverse flow, and this scaling is broken by transverse flow. An accurate comparison of pion and kaon correlations can thus resolve the issue whether the observed $m_\perp$-dependence of the

[1] see Fig. 4.11.

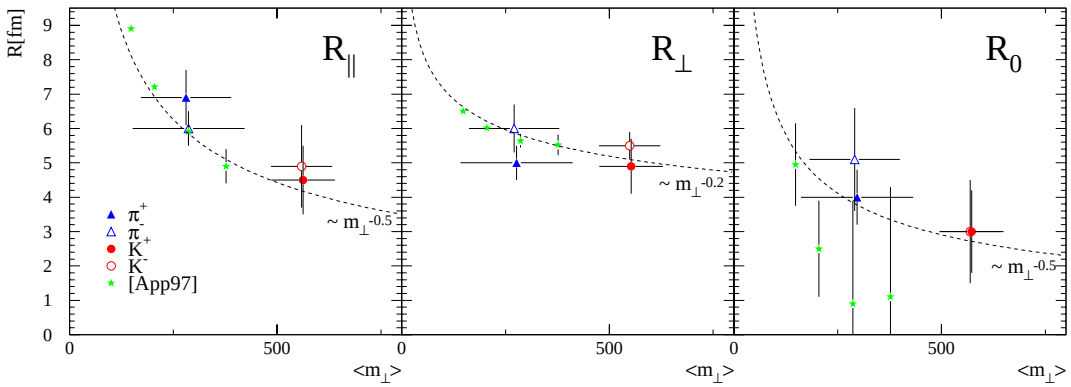

Fig. 6.2: $m_\perp$-dependence of HBT radii using the mean $m_\perp$ in the detector acceptance (see Fig. 6.1).

transverse radius parameter is due to transverse collective flow or other transverse gradients.

For vanishing transverse flow, all three YKP-radii should show perfect $m_\perp$-scaling, i.e. $R_\perp$ remains the same for kaons and pions, $R_{||}$ varies along $m_\perp$. If the source expands longitudinally, $R_{||}$ and R_0 must be smaller for kaon pairs than for pion pairs, even without resonance decays. In the presence of transverse expansion, (a) also the transverse radius $R_\perp$ shows an $m_\perp$-dependence, and the strength of $m_\perp$-dependency is directly related to the magnitude of the transverse flow rapidity. (b) The $m_\perp$-scaling of the YKP radii is broken. The effect is not very large, but it goes in opposite directions for $R_{||}$ and the two other radius parameters.

In our case, the transverse radii of kaons and pions reveal a slight tranverse flow. The longitudinal radii goes consistently almost along the $m_\perp$-scaling, even though they have relatively very large error ranges. This reveals, that the expansion of the source is much stronger in the longitudinal than in the transverse direction.

Taking the freeze-out temperature T$\approx$ 120 MeV [App98] for both particles, one can plot the longitudinal radii as a function of $\sqrt{\frac{T}{m_\perp}}$ as shown in Fig. 6.3. Since the function 2.40 has only one slope parameter τ_f, one obtains **the freeze-out proper time τ_f= 10$\pm$1.5 fm/c for both particles**. In Fig. 6.3 the results from the pion HBT for each K_T-bin [App97] are also plotted. Our results show very good agreement with the values resulted in [Sch97], [App97], [App98], which are obtained

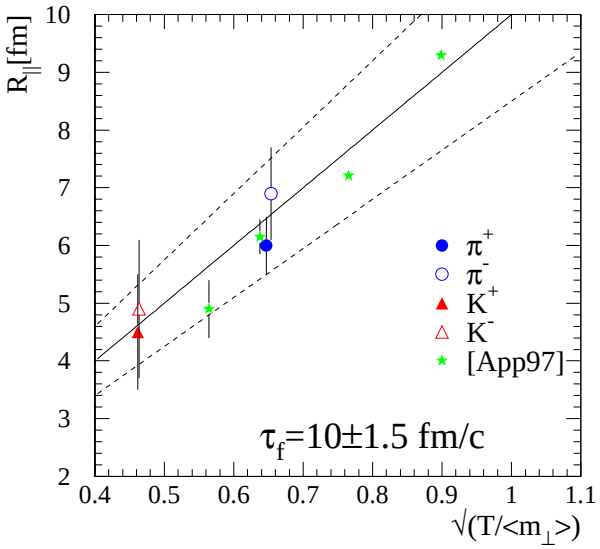

Fig. 6.3: $R_{\parallel}$ as a function of $\sqrt{\frac{T}{m_{\perp}}}$ with the particle freeze-out temperatures T≈ 120 MeV [App98]. The solid and dashed lines are the functions of Eq. 2.40 with the possible slope parameters τ_f. The values from [App97] are also plotted, which are analyzed in each K_T-bin for the pions ($2.9 \leq Y_{\pi\pi} \leq 3.4$).

from the previous pion HBT analyses by $R_{\parallel}$ in the function of K_T-bins.

The relative long freeze-out proper time of 10 fm/c ($\simeq 3.3 \cdot 10^{-23}$ sec) is extracted with the standard deviation of $\sigma_{\tau_f} \equiv R_0 \simeq 4$ fm/c ($\simeq 1.3 \cdot 10^{-23}$ sec) for both particles, and at that time the spatial extentions (one standard deviation) of particle sources are extracted as transversely about the same $R_{\perp} \simeq 5$ fm for both particles and as longitudinally $R_{\parallel} \simeq 4.7$ fm and 6.5 fm for the kaons and the pions, respectively.

6.3 Conclusion and Outlook

As mentioned in section 1.3, an anomalously long lifetime could be a signal of a phase transition that has a latent heat associated with it. Our results are consistent with such a scenario.

With a larger kaon sample than available up to now the transverse expansion could be studied by investigating the $K_\perp$-dependency of $R_\perp$. Production of new NA49 data on central Pb+Pb collisions at 158 AGeV is in progress. TOF-identified kaons from about 3 million events are expected. In addition, with the progress of tracking and $\mathrm{d}E/\mathrm{d}x$ analysis in the MTPC, one could also pick out MTPC kaons at other rapidity ranges with little contamination.
The complete HBT analysis, i.e. the extraction of radii in each $K_\perp$ and rapidity bin of kaons, would deliver detailed informations about the freeze-out configuration for kaons, and the comparison of those for kaons and pions would allow to understand the development of the reaction zone.

Bibliography

[Abb92] T. Abbott et al., Phys. Rev. Lett. **69**, 1030 (1992)

[Act91] P. D. Acton et al. (OPAL Collaboration), Phys. Lett. **B267**, 143 (1991)

[Afa99] S. Afanasiev et al. (NA49 Collaboration), Nucl. Instr. Meth. **A430** (1999) 210

[Afa00] S. Afanasiev et al. (NA49 Collaboration), Phys. Lett. **B491** (2000) 59

[Aki93] W. A. Zajc et al., Phys. Rev. Lett. **70**, 1057 (1993)

[Alb95] T. Alber et al., Phys. Rev. Lett. **75**, 3814 (1995)

[Alb97] T. Alber et al., Z. Phys. **C73**, 443 (1997)

[And87] B. Andersson et al., Nucl. Phys. **B281**, 289 (1987)

[App97] H. Appelshäuser, Dissertation, Univ. of Frankfurt am Main (1997)

[App98] H. Appelshäuser et al. (NA49 Collaboration), Eur. Phys. J. **C2**, 661 (1998)

[Bay96] G. Baym and P. Braun-Munzinger, Nucl. Phys. **A610**, 286c (1996)

[Ber88] G. Bertsch et al., Phys. Rev. **D37**, 1202 (1988)

[Bet32] H. A. Bethe, Ann. Phys. **5**, 325 (1932)

[Bjo83] J. D. Bjorken, Phys. Rev. **D27**, 140 (1983)

[Blo33] F. Bloch, Z. Phys. **81**, 363 (1933)

[Bow91] M. G. Bowler, Phys. Lett. **B270**, 69 (1991)

[Bre85] A. Breakstone et al., Phys. Lett. **162B**, 400 (1985)

[Bre87] A. Breakstone et al., Zeit. Phys. **C33**, 333 (1987)

[Bri95] D. Brinkmann, Dissertation, IKF, Univ. of Frankfurt am Main (1995)

[Cha95a] S. Chapman, P. Scotto, U. Heinz, Phys. Rev. **C52**, 2694 (1995)

[Cha95b] S. Chapman, P. Scotto, U. Heinz, Heavy Ion Physics **1**, 1 (1995)

[Cho74] A. Chodos, R. L. Jaffe, K. Johnson, C. B. Thorn and V. F. Weisskopf, Phys. Rev. **D9**, 3471 (1974)

[Eck96] F. Eckhardt, Dissertation, Univ. of Marburg (1996)

[Fri99] V. Friese, Dissertation, Univ. of Marburg (1999)

[Fri99a] V. Friese, private communication (1999)

[Gaz99] M. Gaździcki, Phys. Rev. **C60**, 054903 (1999)

[Gel64] M. Gell-Mann, Phys. Lett. **8**, 214 (1964)

[Gol60] G. Goldhaber,S. Goldhaber, W. Lee, and A. Pais, Phys. Rev. **120**, 300 (1960)

[Gyu89] M. Gyulassy et al., Report No. LBL 24674 (1989)

[Gyu90] M. Gyulassy et al., Phys. Rev. **C41**, R21 (1990)

[Han54] R. Hanbury-Brown and R. Q. Twiss, Phil. Mag. **45**, 663 (1954)

[Han56] R. Hanbury-Brown and R. Q. Twiss, Nature **178**, 1046 (1956)

[Har98] D. Hardtke and T. J. Humanic, Phys. Rev. **C57**, 3314 (1998)

[Hei96] U. Heinz et al., preprint(nucl-th/9606041) (1996)

[Hen97] T. Henkel, Diplomarbeit, Univ. of Marburg (1997)

[Her95] M. Herrmann and G. F. Bertsch, Phys. Rev. **C51**, 328 (1995)

[Hum88] T. J. Humanic et al., Z. Phys. **C38**, 79 (1988)

[Kop74] G. I. Kopylov, Phys. Lett. **50B**, 472 (1974)

[Las97] B. Lasiuk, Dissertation, pp.25, UCLA (1997)

[Mat86] T. Matsui and H. Satz, Phys. Lett. **B178**, 416 (1986)

[Mak88] A. Makhlin, Y. Sinyukov, Z. Phys. **C39**, 69 (1988)

[Mes91] A. Messiah, Quantenmechanik 1, de Gruyter (1991)

[Moc97] A. Mock, Dissertation, Max-Planck-Institut für Physik, München, MPI-PhE/97-12 (1997)

[Mue85] B. Müller, Lecture Notes in Physics, Vol.225, Springer Verlag (1985)

[Nar92] M. Nardin, W. F. Perger and A. Bhalla, *Algorithm 707. CONHYP: A numerical evaluator of the confluent hypergeometric function for complex arguments of large magnitudes*, ACM Trans. Math. Software **18**, 345-349 (1992)

[PDG98] C. Caso et al. (Particle Data Group), *Particle Physics Booklet*, Springer (1998)

[Pod83] M. I. Podgoretskii, Sov. J. Nucl. Phys. **37**, 272 (1983)

[Pra86] S. Pratt, Phys. Rev. **D33**, 1314 (1986)

[Pra86a] S. Pratt, Phys. Rev. **D33**, 72 (1986)

[Raf82] J. Rafelski, Phys. Rep. **88**, 331 (1982)

[Raf92] J. Rafelski, Nucl. Phys. **A544**, 279c (1992)

[Sch92] J. Schukraft, Nucl. Phys. **A553**, 31c (1992)

[Sch97] S. Schönfelder, Dissertation, Max-Plank Institut Munich (1997)

[Sin89] Y. Sinyukov, Nucl. Phys. **A498**, 151c (1989)

[Sin98] Y. Sinyukov et al., Phys. Lett. **B432**, 417 (1998)

[Son94] P. Sonderegger, CERN PPE/94-21 (1994)

[Ste71] R. M. Sternheimer and R. F. Peierls, Phys. Rev. **B3**, 3681 (1971)

[Sto94] R. Stock, NATO Advanced Research Workshop : Hot Hadronic Matter, Theory and Experiment Proceedings, Divonne-Les-Bains, June 27-July 1, 1994

[Wie96] U. A. Wiedemann, P. Scotto, U. Heinz, Phys. Rev. **C53**, 918 (1996)

[Won94] C. -Y. Wong, *Introduction to High-Energy Heavy-Ion Collisions*, World Scientific (1994)

[Wu98] Y. Wu et al., Eur. Phys. J. **C1**, 599 (1998)

[Yan78] F. Yano, S. Koonin, Phys. Lett. **78B**, 556 (1978)

[Yua96] W. Yuanfang and U. Heinz, preprint(nucl-th/9607037) (1996)

[Zaj84] W. A. Zajc et al., Phys. Rev. **C29**, 2173 (1984)

[Zwe64] G. Zweig, CERN Report Th 401 and Th 402 (1964)